

Full length article

Study of the influence of hydrogen on strain hardening and strain localization in a Fe-19Ni-24Cr austenitic steel through quantitative dislocation structure analysis

Ivan Gutiérrez-Urrutia ^{*} , Yuhei Ogawa , Akinobu Shibata

Research Center for Structural Materials, National Institute for Materials Science (NIMS), 1-2-1, Sengen, Tsukuba 305-0047, Japan

ARTICLE INFO

Keywords:

Hydrogen embrittlement
Strain hardening
Austenitic steels
Dislocation structure

ABSTRACT

The evaluation of hydrogen's impact on key variables of dislocation structures—such as scale and boundary thickness/misorientation—in Fe-Ni-Cr austenitic steels offers deeper insight into the influence of hydrogen on deformation behavior. This understanding can aid in designing steels with enhanced resistance to hydrogen embrittlement. In this study, we examined the interplay among hydrogen, dislocation structure, strain hardening, and strain localization in a Fe-19Ni-24Cr (wt. %) austenitic steel through quantitative dislocation structure analysis. The evaluation of strain hardening by a dislocation-structure-based statistical model clarifies the individual roles of dislocation cells, cell blocks, and dense dislocation walls in the hardening process. We find that the impact of elastic shielding on key variables of dislocation structure and the hardening parameter associated with dislocation-forest hardening is limited, leading to only slight variations in hardening mechanisms. The hardening mechanism most dependent on hydrogen is solid-solution strengthening. Additionally, this study uncovers several hydrogen-related effects associated with the activation of secondary dislocation structures and strain localization at cell block boundaries, proposing a dislocation-based model that correlates the observed phenomena. These results provide a comprehensive understanding of the influence of hydrogen on dislocation-based processes controlling the deformation behavior and hardening in Fe-Ni-Cr austenitic steels.

1. Introduction

Fe-Ni-Cr austenitic stainless steels are widely used in structural components, offering a superior combination of mechanical performance and corrosion resistance in hydrogen environments [1]. However, these steels still experience hydrogen-induced degradation of their mechanical properties associated with hydrogen-induced strain localization [2–7]. The impact of hydrogen on deformation behavior in austenitic steels has been commonly interpreted in terms of the hydrogen-enhanced localized plasticity (HELP) mechanism, based on the elastic shielding of the dislocation's stress field induced by hydrogen [8,9]. Two critical elements of the HELP mechanism can be distinguished: a hydrogen-induced increase in dislocation mobility [10–12] and a hydrogen-induced reduction in dislocation-dislocation interactions [13,14], which facilitates planar slip and stabilizes piled-up configurations that lead to damage initiation [15–17]. Recently, the shielding effect has been linked to variations in dislocation structure and hardening observed in a pure face-centered cubic (fcc) metal, such as Ni,

when exposed to hydrogen. Several studies [13,18,19] have suggested that in this material, the shielding effect reduces the average dislocation cell size by 15 – 75 % [13,19] and decreases the dislocation density at dislocation cell walls by a factor of 2 [13]. Interestingly, Ghermaoui et al. [13] have shown that in Ni, the addition of 7 mass ppm of hydrogen reduces the hardening parameter, α , by 15 %. α accounts for the dislocation forest hardening, given by the Taylor relation $\tau = \alpha Gb \sqrt{\rho}$, where τ is the critical stress for the onset of slip, G is the shear modulus, b is the Burgers vector, and ρ is the average mobile dislocation density [20]. Specifically, α corresponds to the average value of the strength of the dislocation segment formed after the reaction between two dislocations (so-called junction) [21]. The junction lies at the intersection of the two interacting slip planes; it is usually immobile, representing a barrier to dislocation motion. In fcc metals, the strongest junctions correspond to Lomer junctions formed on {0 0 1} planes [22]. Both experimental and theoretical approaches have shown that for an applied stress such that the average mobile dislocation density, ρ , is $\sim 10^{12} \text{ m}^{-2}$, $\alpha = 0.35$ [23,24]. At larger applied stress, α decreases ($\alpha \sim$

^{*} Corresponding author.

E-mail address: gutierrezurrutia.Ivan@nims.go.jp (I. Gutiérrez-Urrutia).

<https://doi.org/10.1016/j.actamat.2026.122078>

Received 28 October 2025; Received in revised form 27 February 2026; Accepted 3 March 2026

Available online 6 March 2026

1359-6454/© 2026 The Authors. Published by Elsevier Inc. on behalf of Acta Materialia Inc. This is an open access article under the CC BY-NC-ND license (<http://creativecommons.org/licenses/by-nc-nd/4.0/>).

0.23 for $\rho \sim 10^{16} \text{ m}^{-2}$). This effect has been associated with the heterogeneous nature of the dislocation arrangement at large deformation stages [24]. The hydrogen-induced reduction of α observed in Ni, combined with a reduction in the average dislocation density of 25–40 % [13], suggests that hydrogen addition can reduce the stability of forest dislocations, weakening the average junction strength. The combination of these hydrogen-related effects can lead to either strain hardening in polycrystalline Ni [18] or strain softening in a single-crystal [0 0 1] Ni [13].

To the knowledge of the authors, the influence of the shielding effect on key variables of the dislocation structure (scale and boundary thickness/misorientation) has not yet been evaluated in Fe-Ni-Cr austenitic steels. This lack of experimental data limits understanding of hydrogen-related effects on strain hardening and the development of Fe-Ni-Cr austenitic steels with superior hydrogen embrittlement (HE) resistance. According to dislocation-based hardening models [25,26], dislocation structure hardening is determined by the dislocation mean free path, defined as the inverse of dislocation length stored per area, and the dislocation boundary hardening parameter. In tensile-deformed fcc polycrystalline materials, the dislocation structure consists of a complex distribution of several dislocation structure types, such as dislocation cells (DCs), cell blocks (CBs), and dense dislocation walls (DDWs) [27–30]. These structures exhibit a characteristic grain-orientation dependence along the main tensile deformation texture components (DCs: grains oriented close to [0 0 1]//TA directions; DDWs: grains oriented close to [1 1 1]//TA directions; CBs: grains oriented along the line between [1 1 2] and [0 0 1]//TA directions; TA: tensile axis). Accordingly, the evaluation of the impact of the shielding effect on the dislocation structure in Fe-Ni-Cr austenitic steels requires a statistical analysis of the variables of the different dislocation structure types (DCs, CBs, and DDWs).

Besides the previously described aspects, hydrogen addition in Fe-Ni-Cr austenitic steels promotes strain localization along characteristic dislocation structures. At low strain levels ($\epsilon < 0.1$), strain localization occurs along slip bands [2–7] and deformation bands [6]. These effects can contribute to damage accumulation by assisting void and micro-crack formation, thereby promoting hydrogen embrittlement (HE). At high strain levels ($\epsilon > 0.3$), our study of a Fe-30Mn-6.5Al-0.3C (wt. %) austenitic low-density steel has shown that complex strain localization phenomena induced by hydrogen can occur [31]. Hydrogen-induced strain localization along cell blocks and deformation bands can lead to the nucleation of microbands (layer-type dislocation structures with a thickness of 100–200 nm aligned along {1 1 1} crystallographic slip planes), enabling the accommodation of dislocation plasticity (hydrogen-enhanced microbanding effect [31]). These studies suggest that detailed characterization of the dislocation structure associated with strain localization is required to understand the interplay between hydrogen-related strain accommodation and deformation behavior in Fe-Ni-Cr austenitic steels.

The aim of this study is the investigation of hydrogen-related effects on the dislocation structure, strain hardening behavior, and strain localization of a mechanically and thermodynamically stable Fe-Ni-Cr austenitic steel. For this purpose, we selected the Fe-19Ni-24Cr (wt. %) austenitic steel due to its moderate stacking fault energy ($\sim 42 \text{ mJ/m}^2$ [32]), which ensures the mechanical stability of austenite and prevents $\gamma(\text{fcc}) - \epsilon(\text{hcp}) / \gamma(\text{fcc}) - \alpha'(\text{bcc})$ martensitic transformation, and the well-defined crystallographic orientation dependence of the dislocation structure, consisting of DCs, CBs, and DDWs [28,30]. Statistical analyses of the variables of the dislocation structure and hardening parameters are performed by quantitative characterization of the dislocation structure along the main tensile deformation texture components using a combined electron channeling contrast imaging (ECCI), electron backscatter diffraction (EBSD), and scanning transmission electron microscopy (STEM) approach [31,33]. The influence of hydrogen on the hardening associated with dislocation structures is evaluated by a dislocation structure-based model that considers the grain orientation

dependence of dislocation structures [25]. In particular, the impact of the shielding effect on the hardening parameter α is quantitatively evaluated. This study also provides further insights into the interplay among hydrogen-induced strain localization, dislocation structures, and slip behavior, leading to a wider view of the influence of hydrogen-related effects on the deformation behavior of Fe-Ni-Cr austenitic steels.

2. Materials and methods

2.1. Experimental techniques

The steel investigated in the present study was a commercially available Fe-19Ni-24Cr (wt. %) austenitic steel (Type 310S). Details of the processing procedure can be found in [34,35]. Fig. 1(a) shows an inverse pole figure (IPF) EBSD map along the forging direction (FD) of the initial microstructure (uncharged condition). ND1 and ND2 correspond to normal directions to FD. The microstructure contains a large population of annealing twins, which is typical of Fe-Ni-Cr austenitic steels [36]. The selected Fe-19Ni-24Cr steel exhibits both mechanical and thermodynamic stability, resulting in a single-phase austenitic steel [34,35]. The grain size distributions for the uncharged and hydrogen-charged samples are plotted in Fig. 1(b, c). The plots indicate that the grain size distribution is similar in both conditions, with a range of 30–70 μm (annealing twin boundaries are not considered in the grain size analysis). Accordingly, potential grain size effects on plasticity associated with strain-induced compatibility conditions occur at the same statistical rate in both samples. The mechanical tests were conducted using a cylindrical specimen with a diameter of 6 mm at an initial strain rate of $5 \times 10^{-5} \text{ s}^{-1}$ in laboratory air at 295 K. The tensile samples were cut so that the tensile axis (TA) is parallel to FD. Hydrogen charging was performed in a hydrogen gas atmosphere at 270 °C for 200 h and 100 MPa, resulting in a uniform hydrogen content of 133 mass ppm within the sample diameter (estimated by thermal desorption spectroscopy, TDS [34]). No distinctive features were observed in the TDS profile of the hydrogen-charged sample. The analyzed hydrogen content is close to the experimentally available upper limit using conventional pre-charging settings [34].

The central sections of cylindrical-shaped samples cut along the tensile axis were analyzed to exclude surface effects from deformation constraints. The dislocation structures were investigated using an approach consisting of electron channeling contrast imaging (ECCI), electron backscatter diffraction (EBSD), and scanning transmission electron microscopy (STEM). ECCI was performed using a Sigma Zeiss FEG-Scanning Electron Microscope (SEM), Carl Zeiss SMT AG, Germany, equipped with Orientation Imaging Microscopy (OIM) EBSD systems. ECC images were acquired by the EBSD-based ECCI approach described in [37] at 20 kV using a solid-state four-quadrant backscatter electron (BSE) detector at a 5–6 mm working distance. ECCI samples of the central sections of the tensile samples were mechanically polished with 800 and 1200 SiC grit papers and subsequently polished with 9 and 3 μm diamond suspensions. The final polishing was performed with 250 nm colloidal silica suspension (Struers, OP-S). STEM was performed in a JEOL JEM 2800 TEM operating at 200 kV. STEM samples were fabricated in areas of interest using the in-situ focused ion beam (FIB) lift-out method [31] in a Scios 2 ThermoFisher Scientific dual-beam SEM system. This fabrication method ensures that the observation planes used in the STEM and ECCI observations are nearly equal (ECC images were acquired at a tilting range of $\sim 5^\circ$). The FIB approach is shown in Fig. 2. First, the area of interest is analyzed by ECCI (Fig. 2(a)). Subsequently, a protective carbon layer is deposited on the sample surface using a gas-injection system to prevent ion beam damage during milling. Three trenches around the area of interest are fabricated using FIB, producing a cross-section of $20 \times 20 \mu\text{m}^2$ (Fig. 2(b)). In the next step, a micro-manipulator with an attached needle is used to detach the lamella from the sample (Fig. 2(c)). The lifted lamella is finally transferred and

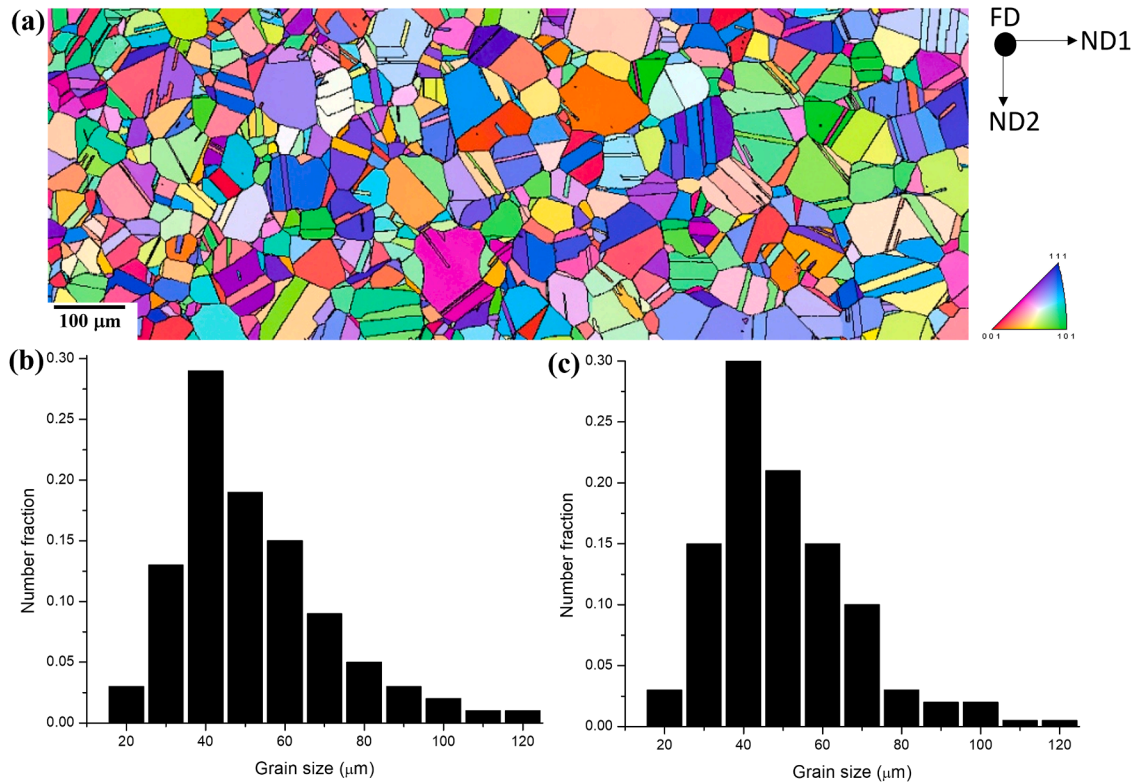


Fig. 1. (a): Inverse pole figure EBSD map along the forging direction (FD) of the initial microstructure (uncharged condition). ND1 and ND2 correspond to normal directions to FD. (b, c): Grain size distributions in the uncharged (a) and hydrogen-charged (b) conditions.

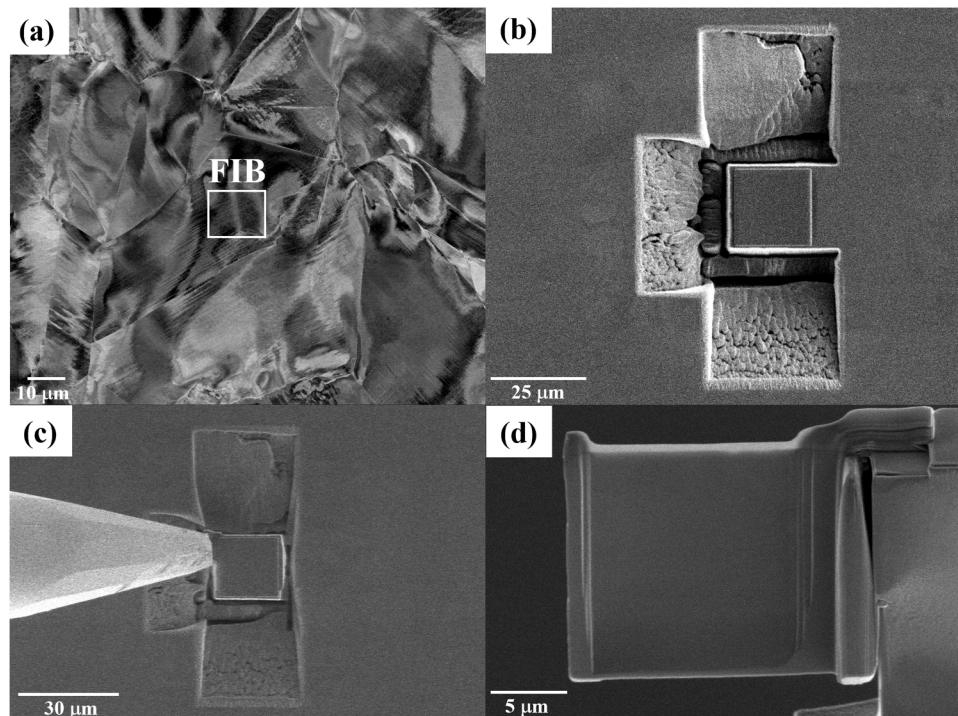


Fig. 2. FIB-based method for STEM lamellae fabrication. (a): ECC image of the area of interest; (b): Milling procedure by FIB; (c): Detachment process of the lamella using a micromanipulator; (d): STEM lamella (thickness ~ 100 nm).

welded to a TEM support grid (Fig. 2(d)). The lamella thinning procedure was performed at an initial acceleration voltage of 30 kV and a milling current of ~ 1000 pA on both sides of the sample, followed by a final thinning procedure at 5 kV and 200 pA to avoid surface damage

induced by FIB milling [38]. No radiation damage (point defects or Ga-rich precipitates) was observed during STEM observations.

2.2. Quantitative dislocation structure characterization

To avoid the effect of local variations in stress state associated with in-grain strain compatibility conditions on dislocation structure variables [39], the dislocation structure formed in the grain interior was quantitatively analyzed. The dislocation structures of the uncharged and hydrogen-charged conditions formed at $\varepsilon = 0.15$ and $\varepsilon = 0.30$ were evaluated on the main components of the tensile deformation texture ($[0\ 0\ 1]//TA$, $[1\ 1\ 1]//TA$, and along the crystallographic line $[1\ 1\ 2] - [1\ 0\ 1]//TA$ (TA: tensile axis)), by the ECCI-EBSD approach developed in [31]. The experimental grain orientations evaluated in uncharged (red dots) and hydrogen-charged (blue dots) conditions are shown in Fig. 3. A total of 35 grain orientations were analyzed at $\varepsilon = 0.15$. 16 grain orientations were analyzed at $\varepsilon = 0.30$. The dislocation structure was classified using the grain orientation dependence introduced by Hansen et al. [27–30]. Type 1 dislocation structure consists of a cell block (CB) structure delimited by geometrically necessary boundaries (GNBs). This type of dislocation structure is developed in grains oriented along the crystallographic line $[1\ 1\ 2] - [1\ 0\ 1]//TA$. Following [31], we classify CBs as Type 1a (one GNB system) and Type 1b (two GNB systems). Type 2 dislocation structure comprises dislocation cells (DCs), formed in grains oriented close to $[0\ 0\ 1]//TA$ directions, where the slip type is octahedral (eight slip systems with similar Schmid factors). Type 3 dislocation structure consists of a combined structure of dense dislocation walls (DDWs) and DCs. This dislocation structure develops in grains oriented close to $[1\ 1\ 1]//TA$ directions, where slip is controlled by three slip systems on two non-coplanar slip planes.

The boundaries of the dislocation structure types were identified on both ECC images and grain reference orientation deviation EBSD maps. The reference point was set as the point with the lowest Kernel average misorientation. 40 to 50 GNBs per grain orientation were analyzed. The total number of GNBs evaluated was about 550 at $\varepsilon = 0.15$ and 175 at $\varepsilon = 0.30$. About 500 DCs per strain level ($\varepsilon = 0.05$, 0.15 , and 0.30) and condition were evaluated. The dislocation boundary misorientation was estimated from EBSD maps. Due to the limited angular resolution of EBSD (0.5° at the current microscope settings and pattern analysis [40]), the boundary misorientation analysis was limited to GNBs. 5 measurements per GNB were performed, resulting in datasets of 875 ($\varepsilon = 0.30$) and 2750 ($\varepsilon = 0.15$) GNB misorientations. The dislocation boundary thickness and spacing were estimated from ECC images using the method shown in Fig. 4. The approach uses the characteristic modulated behavior of the backscattered electron (BSE) intensity associated with channeling contrast of dislocations [41,42] to measure the dislocation configuration boundary parameters. Specifically, Fig. 4 shows an example of the evolution of the BSE intensity profile measured across a DC formed at $\varepsilon = 0.15$ in the hydrogen-charged sample. The modulated behavior of the BSE signal can be explained as follows. Under strong

channeling conditions with $w < 0$ (w : deviation parameter), the BSE intensity collected from the matrix free of dislocations is low (60 – 80 au), due to the strong electron channeling effect (au: arbitrary unit). The BSE intensity collected from the matrix containing a dislocation cell boundary is comparatively high (140 – 240 au), due to the reduced channeling effect induced by dislocations. The parameters t_{DW} (DC wall thickness) and λ_{Di} (DC interior size) are estimated from the corresponding full widths of the modulations of the BSE intensity profile, Fig. 4(b), and considering the projection geometry of the imaged boundary, where the normal direction of the sample, the tilting angle, and the slip plane are determined from EBSD data. In this method, local modulations of lattice rotations can modify the baseline of the BSE signal, thereby contributing to the experimental accuracy of the ECCI approach (1 – 2 nm [41]). To minimize this effect, the average values of the parameters were estimated from 2 – 3 BSE profiles collected per dislocation configuration. The parameters determined by the ECCI method are shown in Table 1.

3. Results

3.1. Mechanical properties

Fig. 5 shows the true stress-strain curves and the evolution of the strain hardening with the stress term $\sigma - \sigma_0$ (σ : true stress; σ_0 : yield stress) of the uncharged and hydrogen-charged samples of the Fe-19Ni-24Cr steel tested at 295 K at an initial strain rate of $5.0 \times 10^{-5} \text{ s}^{-1}$ (a, b) and $5.0 \times 10^{-3} \text{ s}^{-1}$ (c, d). The plots show that at both strain rates, solute hydrogen increases the yield stress (YS), flow stress (FS), ultimate tensile strength (UTS), uniform elongation (UEL), and elongation-to-failure (ETF). The mechanical properties have been analyzed in previous studies [35,43]. The mechanical data show that the influence of the strain rate on mechanical strength is limited. The hydrogen-induced increase in flow stress is 55 – 60 MPa at $5.0 \times 10^{-3} \text{ s}^{-1}$ and 50 – 55 MPa at $5.0 \times 10^{-5} \text{ s}^{-1}$. Our former studies [34,44] have shown that the dynamic interaction between diffusive hydrogen in the material and moving dislocations is the dominant factor governing solid-solution strengthening. This effect arises from the superposition of mechanisms such as a solute-drag effect associated with a hydrogen Cottrell atmosphere and the resistance of the diffusion barrier of hydrogen atoms to follow the dislocation core. Further experimental work is needed to investigate the influence of strain rate on deformation behavior by analyzing dislocation-hydrogen interactions, their contribution to forest hardening, and the evolution of average dislocation density upon straining. In the uncharged condition, our data reveal the activation of three hardening stages, namely stages I, II, and III. The hardening rate of these stages is characterized by a strong decrease in stage I ($\Delta\sigma/\Delta\varepsilon = -66 \text{ MPa}$), a slight decrease in stage II ($\Delta\sigma/\Delta\varepsilon = -2.5 \text{ MPa}$), and a

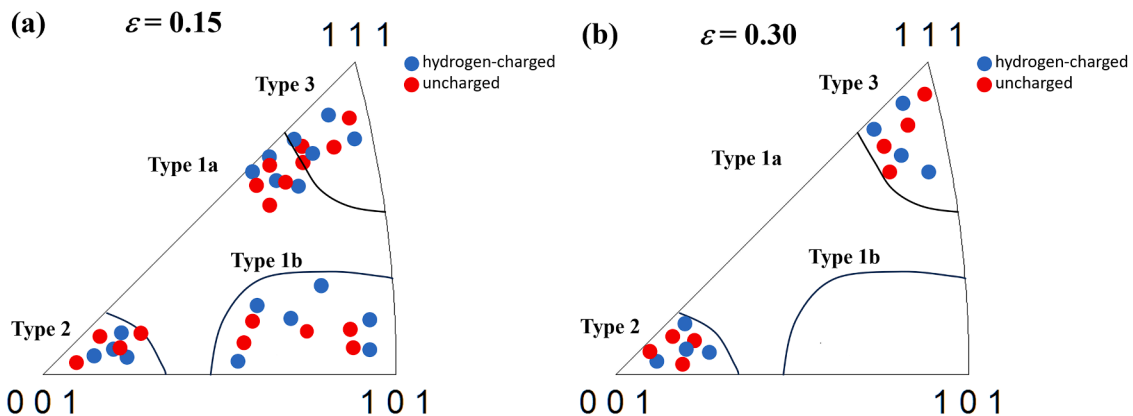


Fig. 3. Inverse pole figures along the tensile axis direction of the experimental grain orientations investigated in the uncharged (red dots) and hydrogen-charged (blue dots) conditions at $\varepsilon = 0.15$ (a) and $\varepsilon = 0.30$ (b).

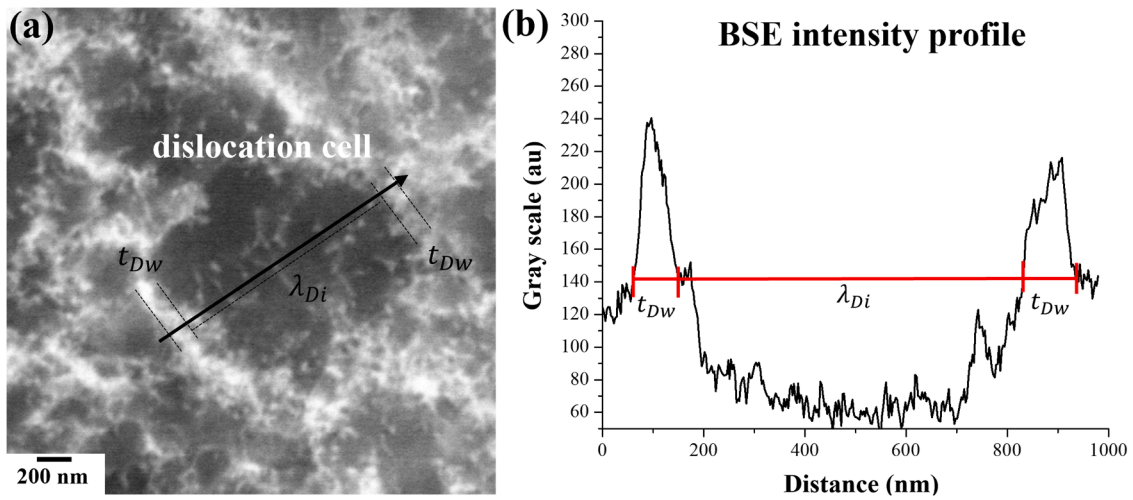


Fig. 4. Analysis method for the determination of dislocation boundary thickness (t_{Dw}) and dislocation boundary spacing of the dislocation structure interior (λ_{Di}). (a): ECC image of a dislocation cell. (b): Backscattered electron intensity profile measured across the dislocation cell imaged in (a).

Table 1

Structural variables of the dislocation structure in the uncharged (UN) and hydrogen-charged (HC) conditions. The error corresponds to the statistical error calculated from the Gaussian regression analysis (Supplementary Materials).

Dislocation structure type	Parameters		
	$\bar{\theta}_{GNB}$	$\bar{\lambda}_{GNB}$ (nm)	\bar{t}_{GNB} (nm)
Type 1a-UN ($\epsilon = 0.15$)	$0.9 \pm 0.2^\circ$	460 ± 125	85 ± 25
Type 1a-HC ($\epsilon = 0.15$)	$1.0 \pm 0.2^\circ$	420 ± 105	90 ± 25
Type 1b-UN ($\epsilon = 0.15$)	$1.1 \pm 0.2^\circ$	710 ± 160	190 ± 40
Type 1b-HC ($\epsilon = 0.15$)	$1.6 \pm 0.2^\circ$	800 ± 175	215 ± 45
Type 2-UN ($\epsilon = 0.05$)	—	655 ± 150	51 ± 10
Type 2-HC ($\epsilon = 0.05$)	—	590 ± 150	47 ± 10
Type 2-UN ($\epsilon = 0.15$)	—	350 ± 65	90 ± 25
Type 2-HC ($\epsilon = 0.15$)	—	305 ± 65	80 ± 25
Type 2-UN ($\epsilon = 0.30$)	—	310 ± 65	110 ± 30
Type 2-HC ($\epsilon = 0.30$)	—	250 ± 65	100 ± 30
Type 3-UN ($\epsilon = 0.15$)	$0.7 \pm 0.1^\circ$	550 ± 110	80 ± 25
Type 3-HC ($\epsilon = 0.15$)	$0.8 \pm 0.1^\circ$	540 ± 110	85 ± 25
Type 3-UN ($\epsilon = 0.30$)	$1.1 \pm 0.1^\circ$	460 ± 105	100 ± 30
Type 3-HC ($\epsilon = 0.30$)	$1.3 \pm 0.1^\circ$	450 ± 110	110 ± 30

moderate decrease before necking ($\Delta\sigma/\Delta\epsilon \sim -5.0$ MPa). The plots reveal that while hydrogen has a small influence on stages I and II, hydrogen addition increases the hardening rate of stage III at the end of its range, from -5 to -2 MPa. This effect produces stage IV hardening.

Microstructural characterization (data included as Supplementary Fig. S1) reveals that deformation twins are formed in both conditions (uncharged and hydrogen-charged) at $\epsilon = 0.3$ (stage III hardening). Specifically, deformation twins are arranged into bundles spaced a few microns, and thereby, their contribution to strain hardening is comparatively smaller than that of the dislocation structure (average size of $250 - 450$ nm, Table 1). Accordingly, hardening stages II and III can be associated with dislocation structure hardening. As shown in our previous study on texture analysis measured by in situ neutron diffraction [43], in the present Fe-19Ni-24Cr steel, hydrogen reduces the strain level required to activate deformation twinning. Specifically, this study shows that hydrogen reduces the strain level at which the area fraction of deformation twins has a noticeable impact on deformation texture, indicating the promotion of deformation twinning. Considering that the impact of a hydrogen content of 133 mass ppm on the twinning stress is negligible (twinning stress scales with stacking fault energy [45] and hydrogen reduces the stacking fault energy by $\sim 6\%$ [32]), the observed hydrogen-induced promotion of deformation twinning can be ascribed to the increased flow stress induced by hydrogen (~ 50 MPa), resulting in enhanced applied stress. This effect promotes deformation twinning

at a lower strain, accelerating the twin kinetics. It is still unclear whether hydrogen influences other aspects of deformation twinning, such as the dislocation-based processes that control twin nucleation and propagation mechanisms. These aspects are currently being investigated. The enhanced deformation twinning activity results in a higher strain hardening rate, due to increased strain accommodation and mechanical stress (twinning-induced plasticity effect [25]), resulting in stage IV hardening (Fig. 5).

Fig. 6 shows the evolution of the deformation texture with strain level for the uncharged and hydrogen-charged samples. The deformation texture in both conditions is characterized by two main components, $\langle 001 \rangle // TA$ and $\langle 111 \rangle // TA$ directions. These texture components remain stable and gradually sharpen upon deformation. In stage III hardening ($\epsilon > 0.15$), $\langle 111 \rangle // TA$ becomes the strongest texture component in both conditions. The plot reveals that at $\epsilon = 0.05 - 0.30$, the intensity of the main texture components is similar in both conditions. This effect indicates that hydrogen plays a small role in the deformation texture. In the following sections, the influence of hydrogen on the key structural variables of the dislocation structures, namely, scale, boundary thickness, and boundary misorientation, is evaluated. The contribution of these variables to strain hardening is quantitatively evaluated in Section 4.

3.2. Dislocation structures

3.2.1. Type 1 dislocation structure

Fig. 7 shows ECC images of Type 1a (a, b) and Type 1b CBs (c, d) dislocation structures in the grain interior formed at $\epsilon = 0.15$ (stage III hardening) in the uncharged (a, c) and hydrogen-charged (b, d) conditions. Type 1a CBs are formed by a set of GNBs lying along the primary slip system [31] (slip system with the highest Schmid factor of 0.42) and secondary slip bands (SBs) formed along non-coplanar secondary slip systems (Schmid factors of 0.37 and 0.27). ECCI analysis of the CB structure in grain orientations forming Type 1a CBs (Fig. 3(a)) indicates the activation of SBs in both conditions (uncharged and hydrogen-charged). Comparatively, SBs in the hydrogen-charged sample have higher dislocation activity, resulting in localized shearing of the CB structure. This process is evaluated in detail in Fig. 8. Type 1b CBs are formed by two GNB sets lying along the two primary slip systems (Schmid factors of 0.47 and 0.5), Figs. 7(c, d). In grains forming these CBs, dislocation plasticity is fully accommodated by the two non-coplanar primary slip systems, resulting in a negligible activation of secondary slip. Accordingly, dislocation plasticity is concentrated along the two GNB sets.

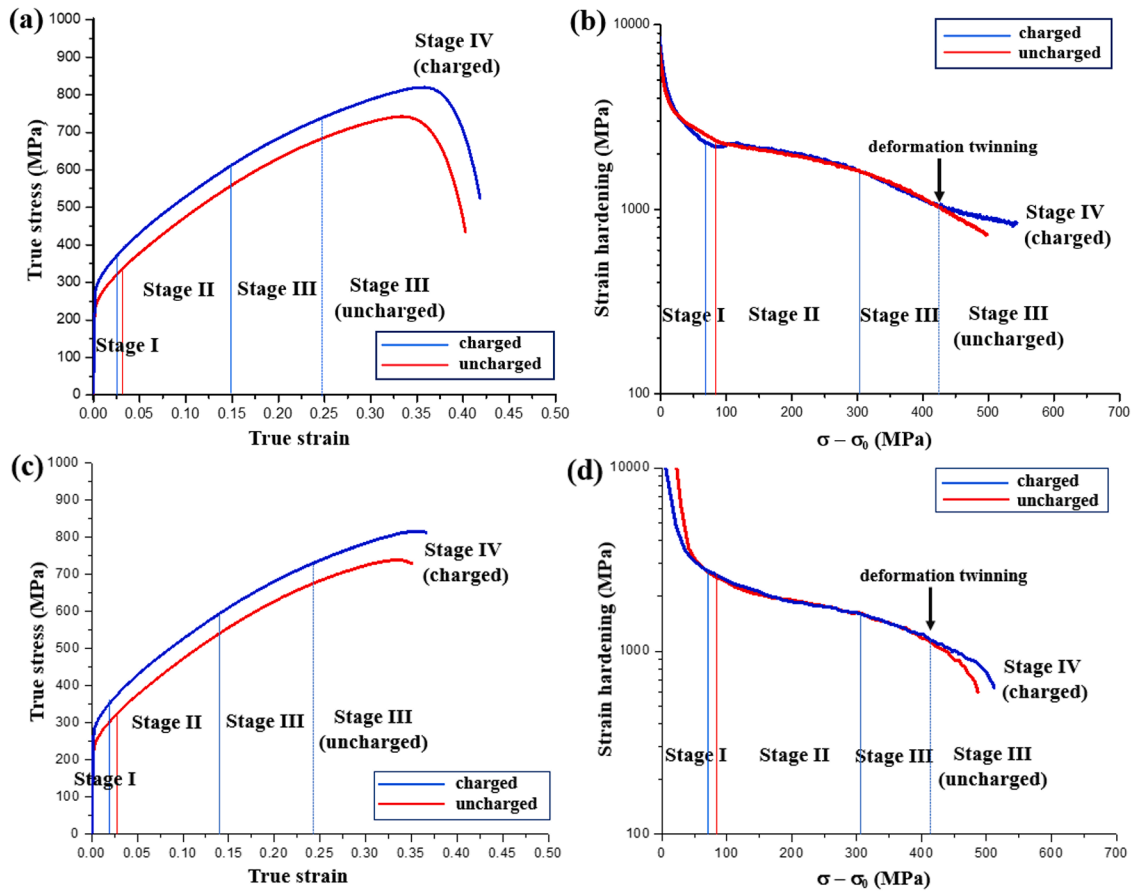


Fig. 5. True stress-strain curves (a, c) and evolution of strain hardening with $\sigma - \sigma_0$ (σ : true stress; σ_0 : yield stress) (b, d) for the uncharged (red lines) and hydrogen-charged (blue lines) conditions in a tensile deformed Fe-19Ni-24Cr steel at an initial strain rate of $5.0 \times 10^{-5} \text{ s}^{-1}$ (a, b) and $5.0 \times 10^{-3} \text{ s}^{-1}$ (c, d) at 295 K.

Fig. 8 analyzes the interactions between secondary SBs and GNBs of Type 1a CBs in the interior of a grain oriented close to the $[9\ 6\ 4]//\text{TA}$ direction (labelled as “G1” in Fig. 8(a)) in the hydrogen-charged sample. The CB structure (Type 1a) is formed by GNBs aligned parallel to the traces of the primary $(-1\ -1\ 1)$ slip plane. The $\{1\ 1\ 1\}$ pole figure calculated from the grain interior (Fig. 8(b)) shows the intensity of lattice rotations about $\langle 1\ 1\ 2 \rangle//\text{TA}$. These lattice rotations are the result of the dominant role of the equivalent highly stressed $(-1\ -1\ 1)$ $[1\ 0\ 1]$ and $(-1\ -1\ 1)$ $[0\ -1\ -1]$ primary slip systems. Examples of the interactions between secondary SBs and primary GNBs are shown in the ECC and STEM images of Fig. 8(c, d). These images were taken from the same region of the grain interior using the sample fabrication method described in Section 2.2. Fig. 8(c) shows the interactions of two SB sets, SB2 and SB3, with primary GNBs. These slip bands are associated with the secondary slip systems $(1\ 1\ 1)$ $[-1\ 0\ 1]$ and $(1\ -1\ 1)$ $[1\ 1\ 0]$ (Schmid factors of ~ 0.30). Interestingly, non-crystallographic shear bands (labeled as “S” in Fig. 8(c)) are also visible. ECCI and STEM analysis indicate that the propagation of secondary SBs and shear bands across the primary dislocation structure results in the localized shearing of GNB sections, indicated by arrows in Fig. 8(c, d). In particular, the propagation of a coarse secondary SB (thickness ~ 300 nm) with a high dislocation density leads to the localized shearing of GNB sections (Fig. 8(d)). These shearing processes produce visible shear offsets in the GNB structure.

Fig. 9 shows the influence of hydrogen on $\bar{\theta}_{\text{GNB}}$ (a, b), $\bar{\lambda}_{\text{GNB}}$, and \bar{t}_{GNB} for Type 1a and Type 1b CBs formed in the grain interior at $\varepsilon = 0.15$ (stage III hardening). The statistical analyses of λ_{GNB} and t_{GNB} are presented in Supplementary Figs. S2 and S3. These parameters were estimated using the ECCI method described in Section 2.2 (Fig. 4) and statistically analyzed using a Gaussian function regression. The standard

deviation of the Gaussian distribution was set as the statistical error. The results indicate that for Type 1a CBs, hydrogen has a negligible effect on $\bar{\theta}_{\text{GNB}}$. We obtain $\bar{\theta}_{\text{GNB}} = 0.9 \pm 0.2^\circ$ and $\bar{\theta}_{\text{GNB}}^H = 1.0 \pm 0.2^\circ$. On the contrary, hydrogen has a significant effect on $\bar{\theta}_{\text{GNB}}$ for Type 1b CBs. From the statistical analysis, we yield $\bar{\theta}_{\text{GNB}} = 1.1 \pm 0.2^\circ$ and $\bar{\theta}_{\text{GNB}}^H = 1.6 \pm 0.2^\circ$. These findings indicate that the grain orientation plays a key role in determining the impact of hydrogen on $\bar{\theta}_{\text{GNB}}$. The analysis also reveals that the grain orientation influences the influence of hydrogen on $\bar{\lambda}_{\text{GNB}}$ and \bar{t}_{GNB} . Specifically, we obtain that hydrogen reduces $\bar{\lambda}_{\text{GNB}}$ of Type 1a CBs by $\sim 9\%$ (from $\bar{\lambda}_{\text{GNB}} = 460 \pm 125$ to $\bar{\lambda}_{\text{GNB}}^H = 420 \pm 105$ nm) and increases $\bar{\lambda}_{\text{GNB}}$ of Type 1b CBs by $\sim 13\%$ (from $\bar{\lambda}_{\text{GNB}} = 710 \pm 160$ to $\bar{\lambda}_{\text{GNB}}^H = 800 \pm 175$ nm). On the other hand, hydrogen increases \bar{t}_{GNB} of both CB types by $\sim 10 - 13\%$. This analysis indicates that hydrogen promotes strain localization along GNBs of Type 1b CBs, resulting in GNB coarsening. This effect is not observed in Type 1a CBs.

3.2.2. Type 2 dislocation structure

Fig. 10 shows ECC images of DCs formed in the grain interior at $\varepsilon = 0.15$ (Figs. 10(a, b)) and $\varepsilon = 0.30$ (Figs. 10(c, d)) in the uncharged (a, c) and hydrogen-charged (b, d) conditions. These strain levels correspond to stages III-IV hardening. DCs exhibit the typical equiaxed morphology of homogeneous distribution. The cell parameters DC interior size (λ_{Di}) and DC wall thickness (t_{Dw}) were quantitatively evaluated using the method described in Section 2.2. The statistical analyses of these parameters are presented in Supplementary Figs. S4 and S5. Fig. 11 plots the evolution of $\bar{\lambda}_{\text{Di}}$ and \bar{t}_{Dw} with strain for the uncharged (red symbols) and hydrogen-charged (blue symbols) conditions. The cell parameters determined at $\varepsilon = 0.05$ (stage II hardening) are also included. We find

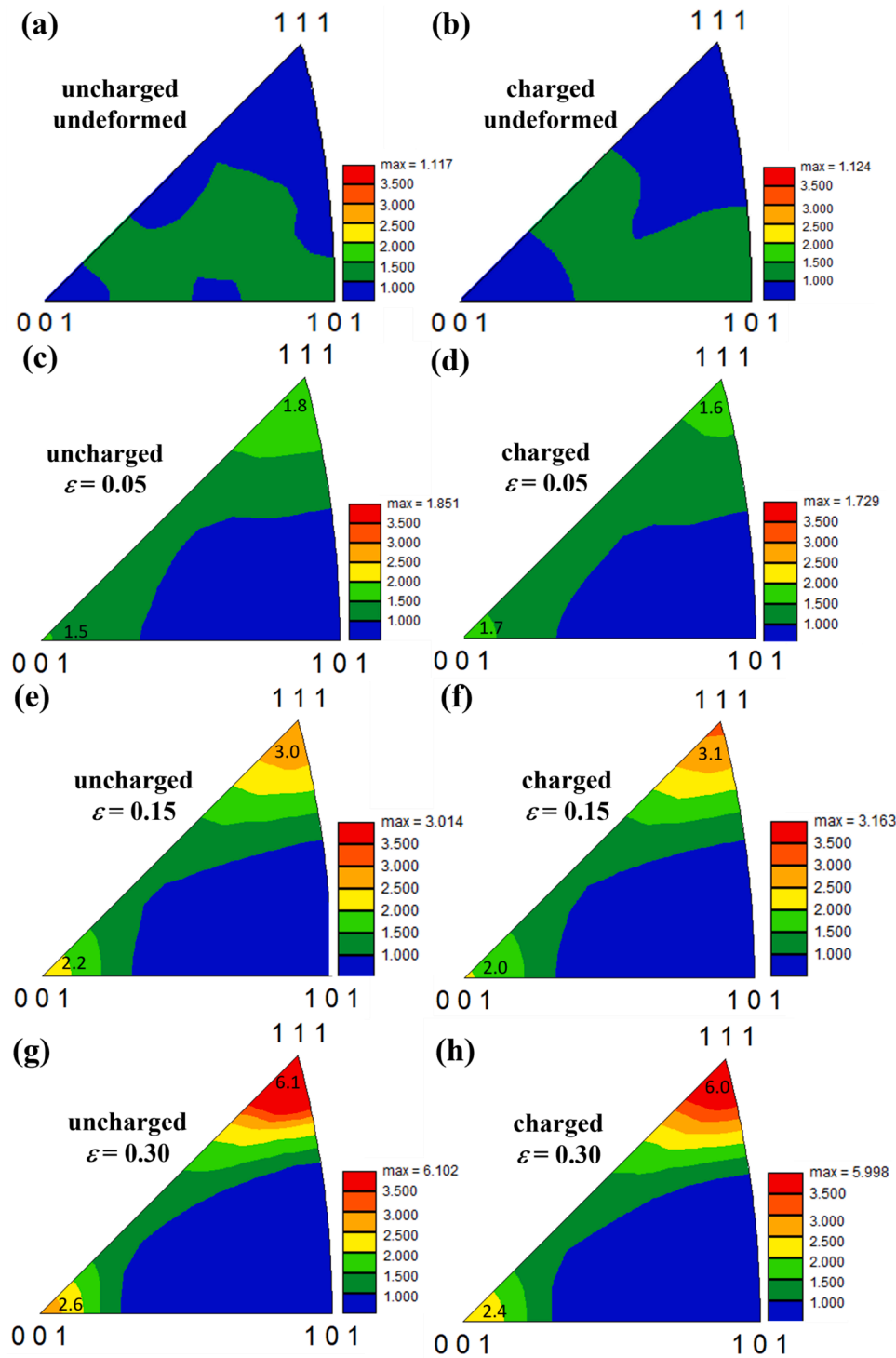


Fig. 6. Evolution of the inverse pole figures (IPFs) along the tensile axis direction with the strain level of a Fe-19Ni-24Cr steel in the uncharged (a, c, e, g) and hydrogen-charged (b, d, f, h) conditions.

that in the strain range $\varepsilon = 0.05 - 0.30$, hydrogen refines $\bar{\lambda}_{Di}$ by 10 – 20 % and $\bar{\varepsilon}_{Dw}$ by 8 – 11 %. These results indicate that the impact of hydrogen on $\bar{\lambda}_{Di}$ is slightly higher than that on $\bar{\varepsilon}_{Dw}$.

3.2.3. Type 3 dislocation structure

Fig. 12 shows ECC images of the Type 3 dislocation structure formed in the grain interior at $\varepsilon = 0.15$ and $\varepsilon = 0.30$, in the uncharged (a, c) and hydrogen-charged (b, d) conditions. These strain levels correspond to stages III-IV hardening. The dislocation structure in the uncharged

condition is mainly formed by a set of dense-dislocation walls (DDWs) lying close to the primary slip plane. Upon deformation, secondary dislocation structures gradually evolve in the uncharged sample (Fig. 12 (c)). ECC images indicate that, comparatively, hydrogen facilitates the formation of secondary dislocation structures that locally shear the DDW structure. This effect is evaluated in Fig. 13. This figure shows the dislocation structures formed at $\varepsilon = 0.15$ in grains oriented close to $[1\ 1\ 1]//TA$ directions in the uncharged (a, b) and hydrogen-charged (c, d) conditions. The analysis of the ECCI (Fig. 13(a)) and STEM (Figs. 13(b-

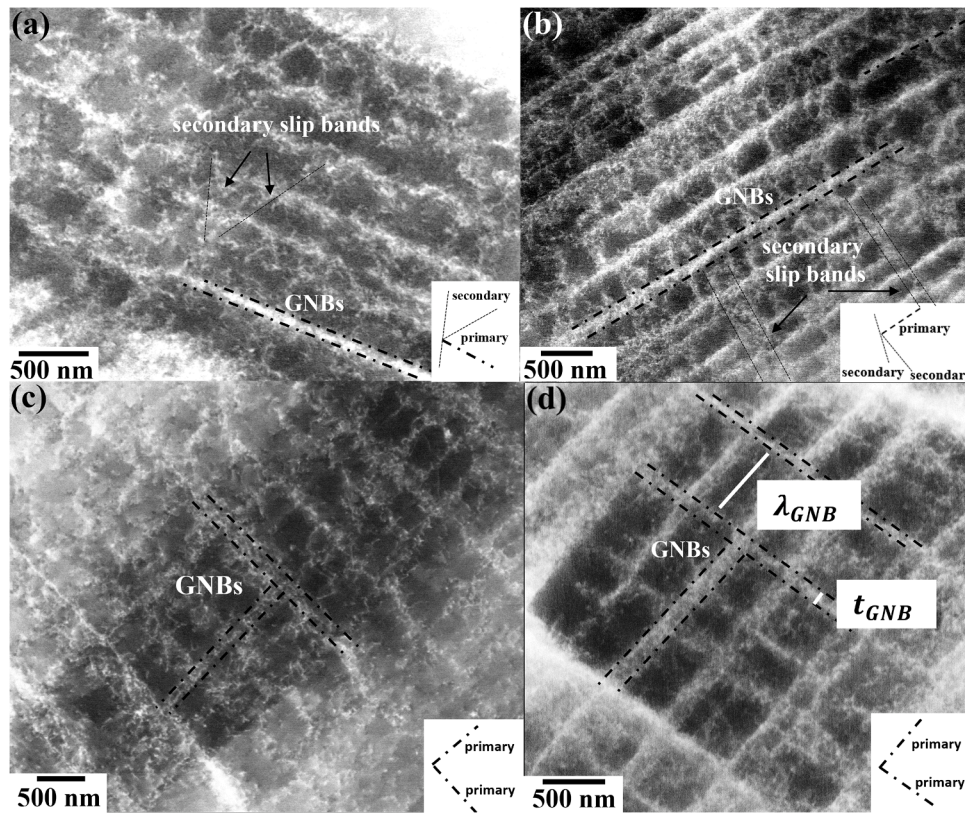


Fig. 7. ECC images of the cell block (CB) structures formed at $\varepsilon = 0.15$ in the uncharged (a, c) and hydrogen-charged (b, d) conditions of a Fe-19Ni-24Cr steel. (a, b): Type 1a CBs; (c, d): Type 1b CBs.

d)) images reveals that in the uncharged condition, the secondary dislocation structures propagating through DDW consist of slip bands formed by discrete dislocations (indicated by “SB” in Figs. 13(a, b)). These observations show that in the uncharged sample, the dislocation activity of the secondary slip bands is limited. In the hydrogen-charged sample, the secondary dislocation structure consists of coarse deformation bands (DBs) with a thickness of $0.50 - 0.75 \mu\text{m}$ (Fig. 13(c)). The interior of DBs includes a high density of loosely arranged dislocations (Fig. 13(d)). These observations indicate that hydrogen enhances plastic accommodation on secondary dislocation structures, resulting in the formation of coarse dislocation structures, such as DBs. The propagation of secondary DBs across the primary DDW structure results in the localized shearing of DDWs, indicating the small mechanical resistance of these structures to the propagation of hydrogen-induced secondary DBs.

The statistical analyses of DDW parameters (λ_{DDW} and t_{DDW}) are presented in Supplementary Figs. S6 and S7. These parameters were estimated using the ECCI method described in Section 2.2 (Fig. 4) and statistically analyzed using a Gaussian function regression. Fig. 14 plots the evolution of $\bar{\lambda}_{DDW}$ and \bar{t}_{DDW} with strain for the uncharged (red symbols) and hydrogen-charged (blue symbols) conditions. We find that at $\varepsilon = 0.15 - 0.30$, hydrogen slightly refines $\bar{\lambda}_{DDW}$ by $\sim 2\%$ and increases \bar{t}_{DDW} by $\sim 6 - 10\%$. The increase in \bar{t}_{DDW} agrees with the increment in $\bar{\theta}_{DDW}$ by $0.1 - 0.2^\circ$ estimated by EBSD. These findings indicate that while the impact of hydrogen on $\bar{\lambda}_{DDW}$ is negligible, hydrogen addition enhances the dislocation activity in the DDW interior, as reflected by the increase in \bar{t}_{DDW} .

4. Discussion

4.1. Influence of hydrogen on dislocation structure

The present study reveals several hydrogen-related effects on the dislocation structure formed in the Fe-19Ni-24Cr austenitic steel. At a hydrogen concentration of 133 mass ppm, the key variables of dislocation structure, such as scale and boundary thickness/misorientation, are modified according to characteristic grain orientation dependences. Fig. 15 plots the average magnitude of the hydrogen-induced variations on the scale of the dislocation structure (a), boundary thickness (b), and boundary misorientation (c) at $\varepsilon = 0.15$ (stage III hardening). Specifically, Fig. 15(a) plots the percentual variation in the average scale of the dislocation structure, $(\bar{\lambda}_i - \bar{\lambda}_i^H)/\bar{\lambda}_i \times 100$, where the superscript “H” corresponds to the hydrogen-charged condition and the subscript “i” designates the type of dislocation structure—CB, DC, and DDW. Fig. 15(b) plots the percentual variation in dislocation boundary thickness, $(\bar{t}_i - \bar{t}_i^H)/\bar{t}_i \times 100$, where the subscript “i” denotes the boundary types IDB and GNB. Fig. 15(c) shows the absolute variation in GNB misorientation, $(\bar{\theta} - \bar{\theta}^H)/\bar{\theta}$, induced by hydrogen. The plots indicate that the influence of hydrogen on the variables of the dislocation structure exhibits a strong dependence on the type of dislocation structure. Specifically, we find that hydrogen reduces the scale ($\bar{\lambda}_i$) of the dislocation structures, except for Type 1b CBs, promotes strain accommodation at GNBs and DDWs (increase of \bar{t}_{GNB} and \bar{t}_{DDW}), and decreases $\bar{\lambda}_{Di}$. These hydrogen-related effects are in line with previous reports in fcc metals, such as Ni, a Ni-16Cr alloy, and an Fe-30Mn-6.5Al-0.3C low-density steel [13,19,31, 46]. However, the magnitude of these effects estimated in the present study is significantly smaller than that reported in previous reports. For example, the hydrogen-induced refinement in $\bar{\lambda}_{Di}$ estimated for the present Fe-19Ni-24Cr steel within the strain range $\varepsilon = 0.05 - 0.30$ is $\sim 10 - 20\%$. This effect is significantly smaller than that reported in Ni,

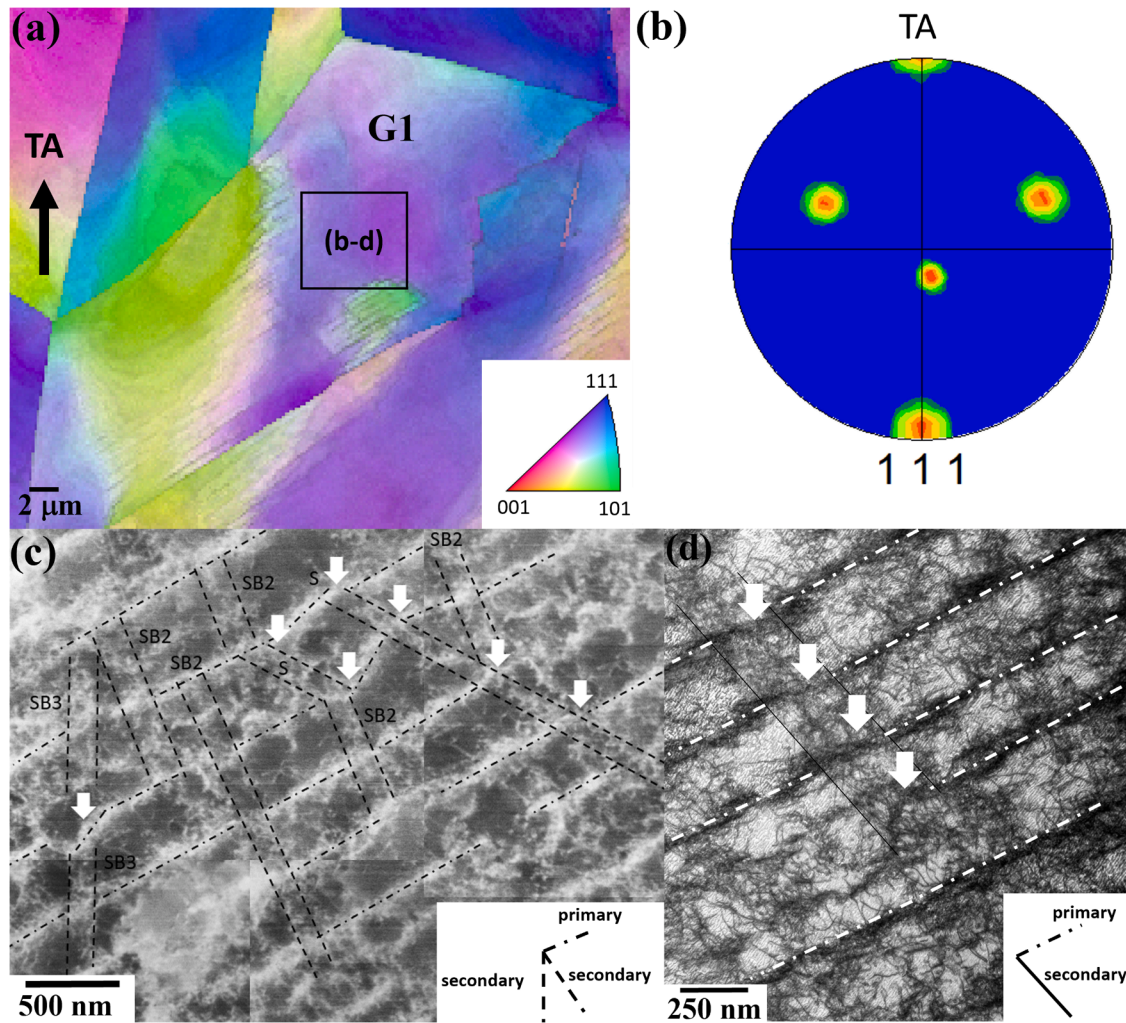


Fig. 8. Detailed analysis of secondary dislocation structures (slip bands, SBs) in a grain forming Type 1a CBs in the hydrogen-charged sample at $\varepsilon = 0.15$. (a) EBSD orientation map (TA: tensile axis); (b) pole figure of the grain marked “G1”; (c) ECC and (d) STEM images of the region surrounded by a rectangle in (a). The white arrows indicate the shearing of the primary dislocation structures by the propagation of secondary slip bands. The signature “S” in (c) denotes the shearing of the primary dislocation structure by slip bands (SB).

where hydrogen addition reduces $\bar{\lambda}_{Di}$ by up to 75 % [13,19,46]. According to the dislocation-based processes controlling DC formation [47–49], $\bar{\lambda}_{Di}$ is determined by the competition between dislocation recombination/annihilation and dislocation trapping/storage processes acting within DCs. These dynamic processes are controlled by dislocation-based reactions assisted by cross-slip and climb. The present results suggest that hydrogen has a limited influence on these processes in the Fe-19Ni-24Cr steel. This finding differs from the strong influence of hydrogen content on the recovery process reported in pure Ni [50] and highlights the role of alloying content on these effects.

The present study also shows that hydrogen has a limited impact on the cell wall structure, reducing \bar{t}_{DW} by 8–10 %. The magnitude of this effect is smaller than that reported in Ni, where a reduction of ~ 15 % has been reported [13]. This finding suggests that alloying content may influence the underlying mechanism associated with this process. Previous studies [13,46,51,52] have suggested that this hydrogen-related effect is associated with the weakening of the interaction between dislocations due to the elastic shielding of the dislocation’s stress field induced by hydrogen. As demonstrated by Ghermaoui et al. [13], the impact of hydrogen on the interaction between dislocations has a direct influence on the hardening parameter, α , responsible for the dislocation forest-type hardening: $\tau_{forest} = \alpha G b \sqrt{\rho}$, where G is the shear modulus, b is the Burgers vector, and ρ is the average dislocation density [20]. α

corresponds to the average value of the strength of the dislocation segment formed after the reaction between two dislocations (so-called junction) [21]. This parameter can be estimated from the quantitative analysis of $\bar{\lambda}_{Di}$ and \bar{t}_{DW} , as follows. First, we have to consider that α is related to the cell similitude constant, K , by the relation [23,53]:

$$K/\alpha = \bar{\lambda}_{DC} \sqrt{\rho} \sim 25 \pm 2 \quad (1)$$

where $\bar{\lambda}_{DC} = \bar{\lambda}_{Di} + \bar{t}_{DW}$, and K is given by the hardening relation (the so-called similitude principle) [54,55]:

$$K = (\tau - \tau_0) \bar{\lambda}_{DC} / Gb \quad (2)$$

where τ is the applied shear stress and τ_0 is the matrix friction shear stress. Using eq. (2) and the values of $\bar{\lambda}_{Di}$ and \bar{t}_{DW} estimated at $\varepsilon = 0.05$, 0.15, and 0.30 (Table 1), we can calculate K for the uncharged and hydrogen-charged conditions. The tensile stresses were converted to shear stresses, assuming an average Taylor factor of $M = 2.45$ (Taylor factor of cell-forming grains). As shown in our former study [43], the influence of 133 mass ppm solute hydrogen on G is negligible, hence, $G^H = G$. Using $\tau_0 = 71$ MPa [56], $\tau_0^H = 94$ MPa [35], $G = 80$ GPa [35], and $b = 0.25$ nm [35], we obtain $K = 3.8$ (uncharged condition) and $K^H = 3.6$ (hydrogen-charged condition). The correlation coefficients obtained

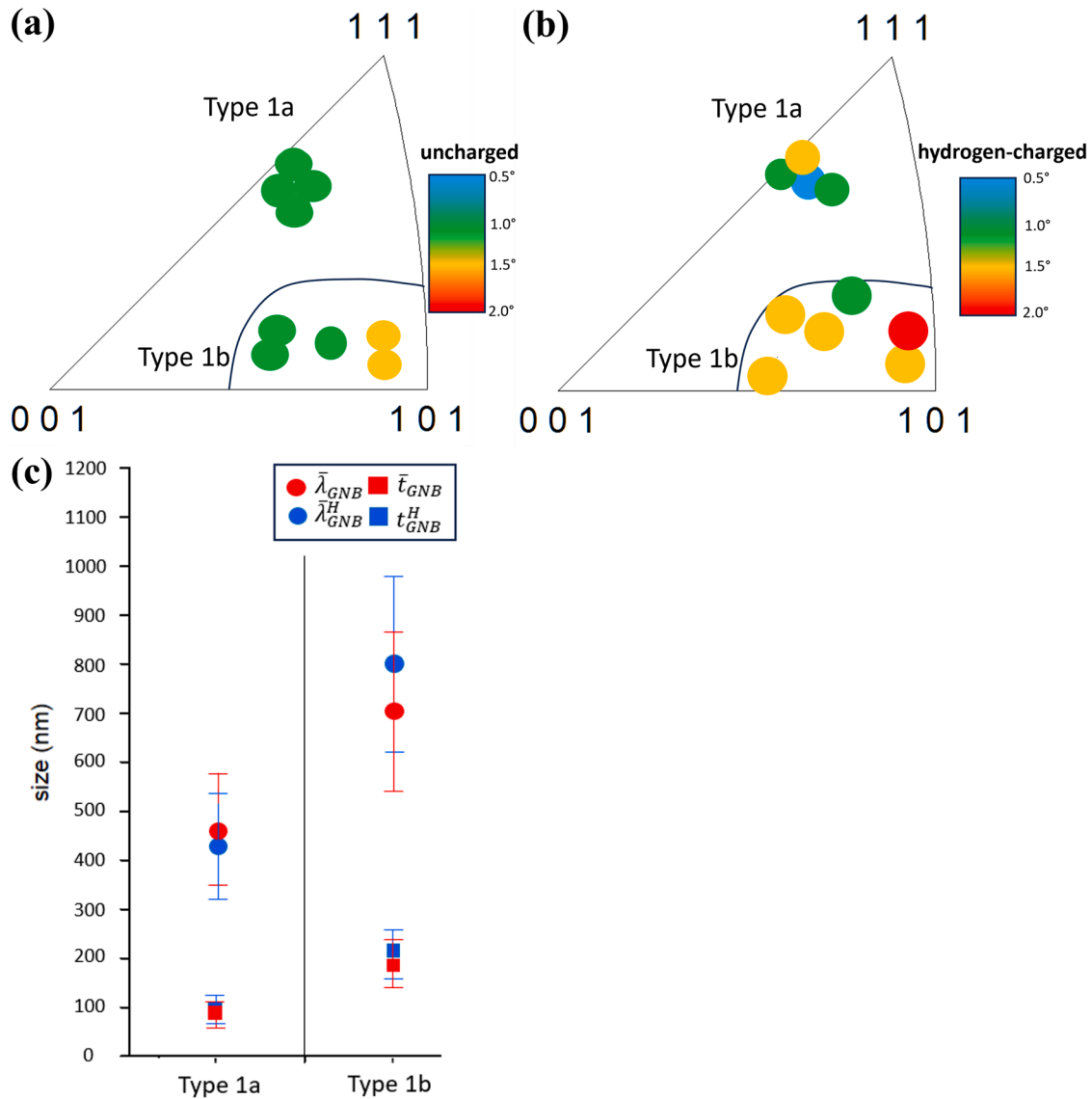


Fig. 9. Influence of hydrogen on the structural variables $\bar{\theta}_{GNB}$ (a, b), $\bar{\lambda}_{GNB}$ (c), and \bar{t}_{GNB} (c) of Type 1a and Type 1b dislocation structures at $\varepsilon = 0.15$. $\bar{\theta}_{GNB}$: average GNB misorientation; $\bar{\lambda}_{GNB}$: average GNB spacing; \bar{t}_{GNB} : average GNB thickness.

from the linear fitting are 0.96 and 0.98, respectively. These values are in the range of K -values obtained for fcc metals with similar normalized stacking fault energies ($\gamma_{SFE}/Gb \sim 2$) to that of the Fe-19Ni-24Cr steel, such as Fe-22Mn-0.6C ($K = 3.7$ [25]), and Fe-12Ni-17Cr ($K=2.9$ [57]). Using Eq. (1) and the estimated values of K and K^H , we obtain $\alpha=0.15$ and $\alpha^H=0.14$. This analysis indicates that hydrogen has a small effect on the hardening parameter, α , reducing its value by 7 %.

The results of the former analysis provide valuable scaling and hardening parameters for dislocation substructure-based models of strain hardening and crack tip plasticity in austenitic steels [25,58,59], which are currently lacking. Specifically, this study indicates that under current hydrogen-charging and deformation conditions, the elastic shielding effect in the Fe-19Ni-24Cr steel has a limited impact on the long-range elastic interaction between dislocations, and thereby, the stability of forest dislocations is slightly altered. As a consequence, the average junction strength that determines the value of the hardening parameter α is not modified by the addition of hydrogen. This finding agrees with a recent study on a single-crystal austenitic Fe-Ni-Cr steel (316 L) [4]. However, it differs from that in a pure fcc metal, such as Ni, where the shielding effect has a strong influence on the dislocation structure and dislocation-dislocation interactions, resulting in a

reduction in α by 25 % [13]. It is worth noting that the shielding effect is based on the Cottrell-Eshelby theory of dislocation-solute interactions [8,9], which does not account for solute-solute interactions [22]. In this theory, the concentration profile of the Cottrell atmosphere corresponds to the equilibrium state of an infinitesimal concentration of Eshelby inclusions with a dilatational misfit in an isotropic elastic solid. As shown by Nowak et al. [60], solute-solute interactions in multicomponent alloys can reduce the concentration profile of a hydrogen atmosphere around a dislocation, thereby limiting the impact of the shielding effect on dislocation forest-hardening, hence, on the parameter α . Further computational work is needed to evaluate the impact of solute-solute interactions on the shielding effect in Fe-Ni-Cr steels. These calculations can provide further understanding of the interplay between alloying content and hydrogen-related effects associated with the shielding effect.

4.2. Influence of hydrogen on strain localization phenomena

The present study reveals interesting features of the interplay between strain localization and the dislocation structure. In CB-forming grains, our analysis indicates that hydrogen promotes the coarsening

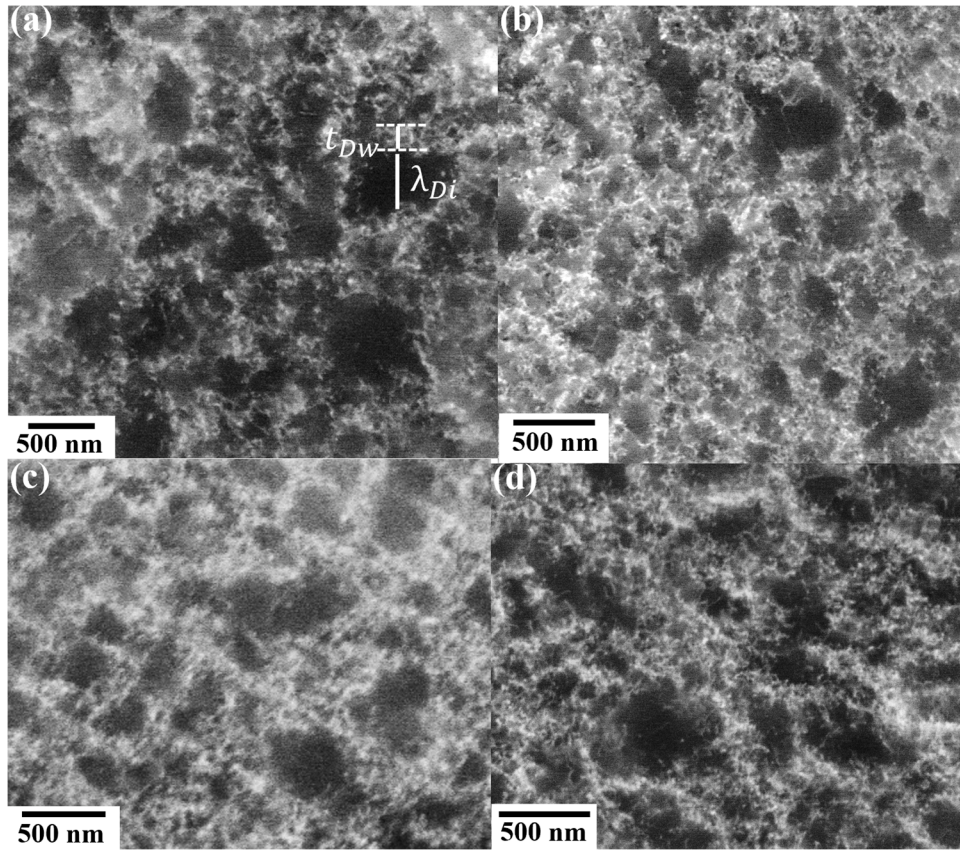


Fig. 10. ECC images of the dislocation cell (DC) structures formed at $\varepsilon = 0.15$ (a, b) and $\varepsilon = 0.30$ (c, d) in the uncharged (a, c) and hydrogen-charged (b, d) conditions of a Fe-19Ni-24Cr steel. λ_{Di} : cell interior size; t_w : cell wall thickness.

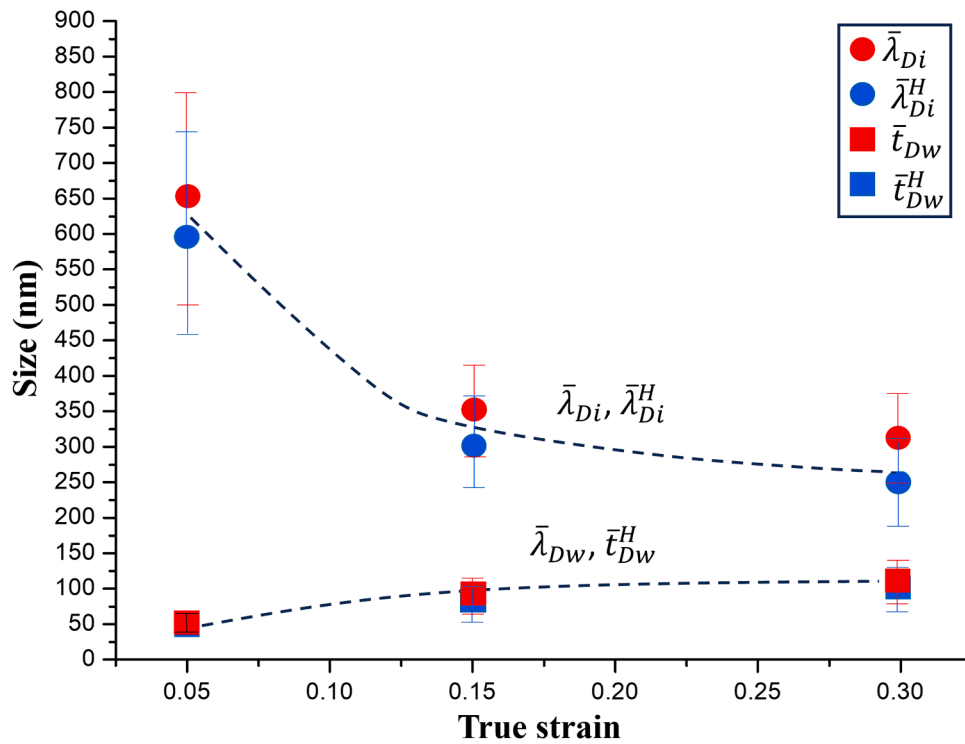


Fig. 11. Evolution of the structural variables $\bar{\lambda}_{Di}$, $\bar{\lambda}_{Di}^H$, \bar{t}_w , and \bar{t}_w^H of Type 2 dislocation structures as a function of strain.

of CB boundaries by $\sim 12\%$. This effect is associated with an increase in the density of geometrically necessary dislocations stored at CB

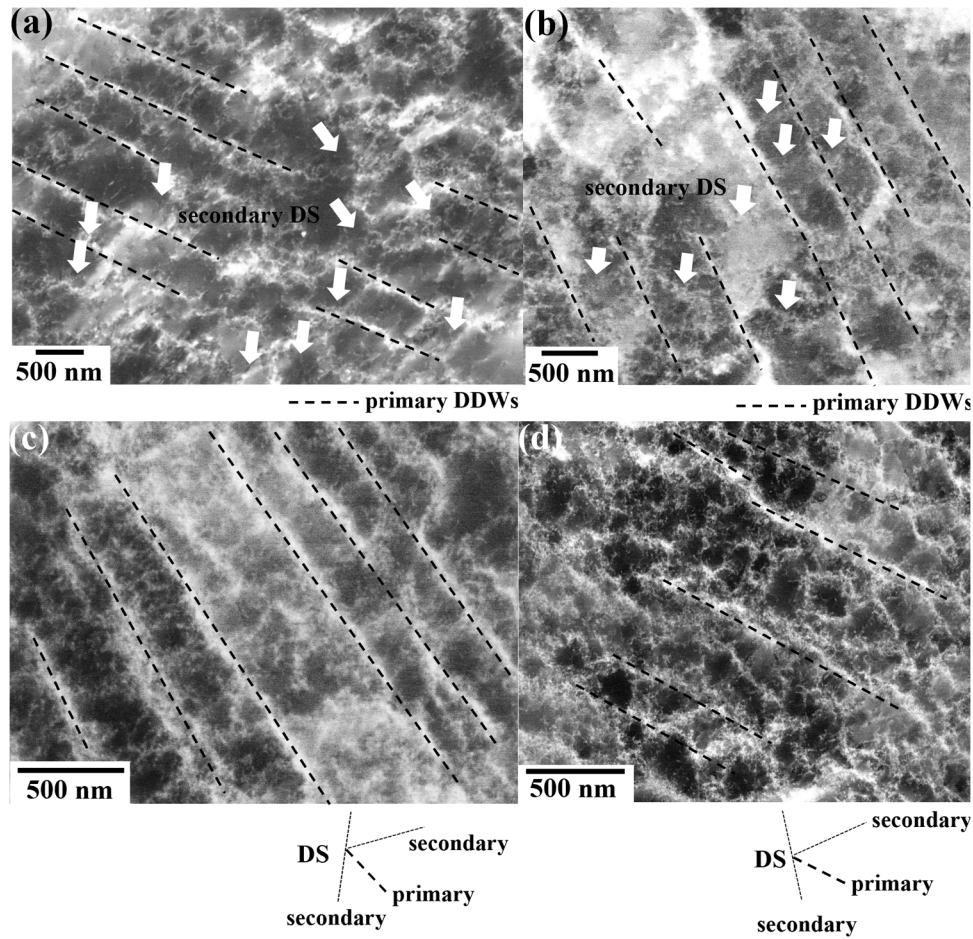


Fig. 12. ECC images of the dense dislocation wall (DDW) structures formed at $\varepsilon = 0.15$ (a, b) and $\varepsilon = 0.30$ (c, d) in the uncharged (a, c) and hydrogen-charged (b, d) conditions of a Fe-19Ni-24Cr steel. DS: dislocation structure.

boundaries, as reflected by the larger CB misorientations measured in the hydrogen-charged condition ($\bar{\theta}_{GNB} = 1.1 \pm 0.2^\circ$; $\bar{\theta}_{GNB}^H = 1.6 \pm 0.2^\circ$). Interestingly, the analysis reveals that while hydrogen reduces $\bar{\lambda}_{GNB}$ of Type 1a CBs, it has an opposite effect on $\bar{\lambda}_{GNB}$ of Type 1b CBs. The influence of hydrogen on the structure of Type 1b CBs observed in this study exhibits similar behavior to the slip localization effect reported in austenitic stainless steels [2–5]. Accordingly, it is worth analyzing the slip behavior of CB-forming grains. In grains forming Type 1a CBs, slip is distributed into several slip systems, namely, a primary slip system and one/two secondary slip systems (Fig. 7(a, b)). This slip behavior is similar to that occurring in grains forming Type 2 (DCs) and Type 3 (DDWs) dislocation structures. The effect of hydrogen on the spacing of Type 1a CBs is hence similar to that observed on these dislocation structures. However, in grains forming Type 1b CBs, slip is concentrated on two primary non-coplanar slip systems with high Schmid factors (~ 0.50). Secondary slip systems are not activated in these grains (Figs. 7(c, d)). In these grains, the addition of hydrogen enhances dislocation activity on the two slip systems, producing a larger CB boundary coarsening. This analysis highlights the effect of slip class on strain localization. Regarding the impact of the previously analyzed strain localization phenomena on damage, it is worth noting that this deformation process occurs in grain orientations that are unstable upon tensile deformation (Fig. 6); hence, its activity is limited to early deformation stages. The contribution of the hydrogen-induced strain localization mechanism associated with Type 1b CB boundary coarsening to the later deformation stages and hence, damage is likely to be limited. This analysis aligns with the fracture behavior examined in our previous study [43], indicating that hydrogen addition does not alter the

ductile fracture mechanism associated with micro-void coalescence and growth.

The present study also highlights an interesting hydrogen-related effect on secondary slip. Our analysis reveals that in grains forming elongated dislocation structures (CBs and DDWs), hydrogen promotes the formation of secondary dislocation structures, such as slip bands and deformation bands (DBs). The quantitative analysis of CB boundary parameters (Fig. 9(c)) indicates that hydrogen promotes the accommodation of strain at CB boundaries, favoring strain localization. This effect has been recently observed in a Fe-30Mn-6.5Al-0.3C austenitic low-density steel, associated with the localized nucleation of microbands at CB boundaries [31]. Although the hydrogen-related mechanisms promoting these effects are still not well understood, the analysis performed in Section 4.1 indicates that the observed hydrogen-induced strain localization phenomena cannot be ascribed to the shielding effect. Recent studies have proposed alternative mechanisms, such as hydrogen-induced variations in dislocation mobility associated with the cross-slip rate and critical resolved shear stress [4,61,62], and hydrogen-induced effects on the long-range stress field of dislocations related to grain-boundary effects on hydrogen segregation [63]. In this study, we suggest a correlation between the hydrogen-induced strain accommodation process occurring at primary GNBs (Fig. 9(c)) and the activation of secondary slip sources, which trigger the secondary dislocation structures observed by ECCI (Figs. 12, 13). The proposed model is depicted in the sketch of Fig. 16.

Previous studies [64,65] have demonstrated that localized stress fluctuations associated with the long-range dislocation field can promote secondary slip. The model depicted in Fig. 16 proposes that

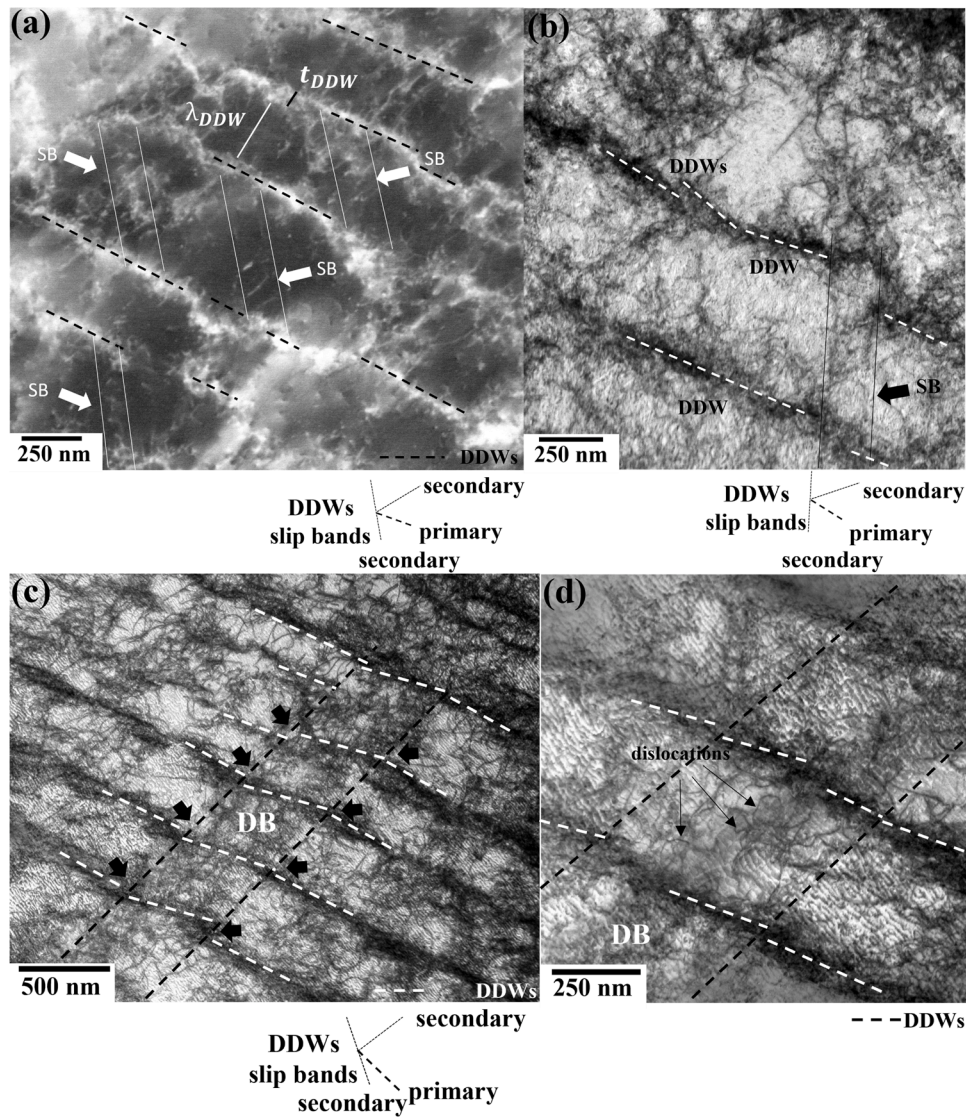


Fig. 13. Analysis of secondary dislocation structures (slip bands, SBs, and deformation bands, DBs) formed at $\epsilon = 0.15$ in grains oriented close to $[1\ 1\ 1]//TA$ directions in the uncharged (a, b) and hydrogen-charged conditions (c, d). (a): ECC image; (b-d): STEM images. DDWs: Dense dislocation walls.

hydrogen-induced strain localization at primary GNBs associated with reduced dislocation spacing ($d_2 < d_1$) leads to localized variations in the stress acting on dislocation sources of secondary slip located along GNBs, resulting in localized dislocation pile-up emission, Fig. 16(a). With further straining, the piled-up dislocation configurations evolve into secondary slip bands (SLBs) and DBs, producing strain localization (Fig. 16(b)). The propagation of these structures across the existing dislocation structure leads to the local shearing of GNBs (Fig. 8(c, d) and 13(c, d)). This effect suggests that the mechanical resistance of DDWs to SLB propagation is small, limiting their contribution to hardening. Upon further straining, dislocation plasticity can be accommodated along the secondary dislocation structures propagating throughout the grain interior. The hydrogen-induced activation of secondary slip has been recently observed in a single-crystal austenitic Fe-Ni-Cr steel (316 L) [4] and a Ni-based superalloy [66]. Further experimental work is needed to evaluate the contribution of hydrogen-induced secondary dislocation structures to the deformation behavior and hardening of Fe-Ni-Cr steels.

4.3. Influence of hydrogen on strain hardening

The characterization of the deformation structure confirms that the strain hardening of the Fe-19Ni-24Cr steel is mainly determined by the

contribution of dislocation structures to hardening, due to the relatively low twin area fraction ($\sim 5\%$ at $\epsilon = 0.35$ [43]). This deformation behavior is typical for medium-stacking fault energy (γ_{SFE}) metals [28, 30] ($\gamma_{SFE} \sim 42\text{ mJ/m}^2$ for Fe-19Ni-24Cr [32]). Hydrogen promotes deformation twinning at the later deformation stages ($\epsilon > 0.20\text{--}0.25$), resulting in a higher strain hardening rate (twinning-induced plasticity effect [25]), and the activation of an additional hardening stage, stage IV hardening (Fig. 5). Our recent study [32] has shown that the addition of 133 mass ppm of solute hydrogen slightly reduces γ_{SFE} by 6 %. Accordingly, the activation of γ_{SFE} -dependent processes, such as $\gamma(\text{fcc}) - \epsilon(\text{hcp})/\gamma(\text{fcc}) - \alpha'(\text{bcc})$ martensitic transformation, is not promoted by hydrogen addition, as evidenced in [43]. In this section, we evaluate the contribution of dislocation structures (DCs, CBs, and DDWs) to hardening by a statistical model based on the MFP approach [67–70]. Following former approaches [25,26], the contributions of the different types of dislocation structures to the strain hardening can be written as:

$$\sigma = \sigma_0 + f_{DC} \sigma_{DC} + f_{CBa} \sigma_{CBa} + f_{CBb} \sigma_{CBb} + f_{DDW} \sigma_{DDW} \quad (3)$$

where σ_0 is the matrix friction stress, and f_{DC} , f_{CBa} , f_{CBb} , and f_{DDW} are the fractions of the grains forming DCs, Type 1a CBs, Type 1b CBs, and DDWs, respectively. In this approach, the effect of long-range back

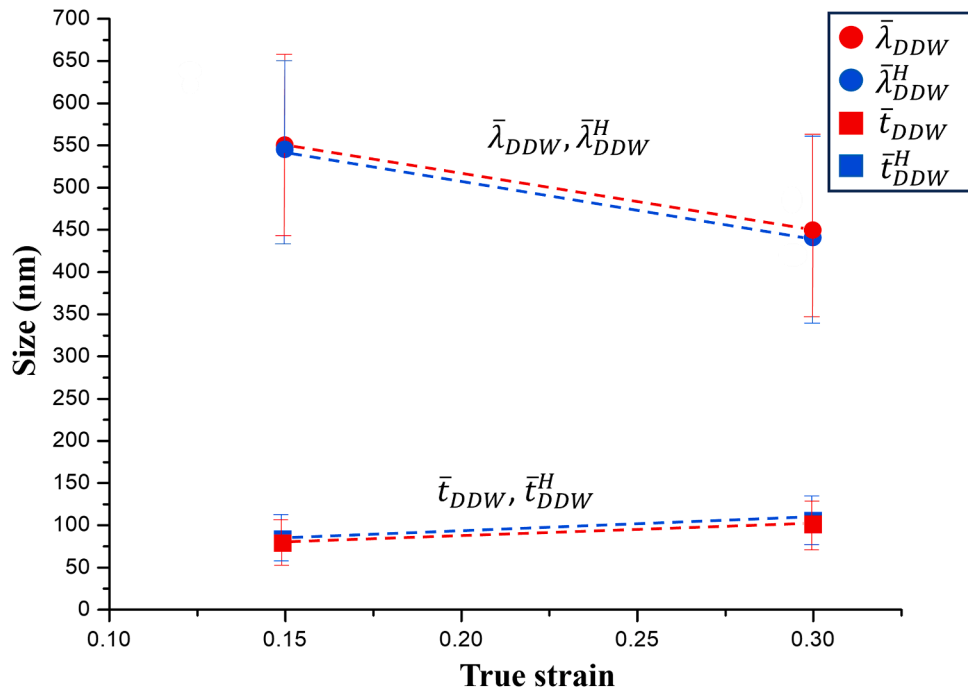


Fig. 14. Evolution of the structural variables $\bar{\lambda}_{DDW}$, $\bar{\lambda}_{DDW}^H$, \bar{t}_{DDW} , and \bar{t}_{DDW}^H of Type 3 dislocation structures as a function of strain.

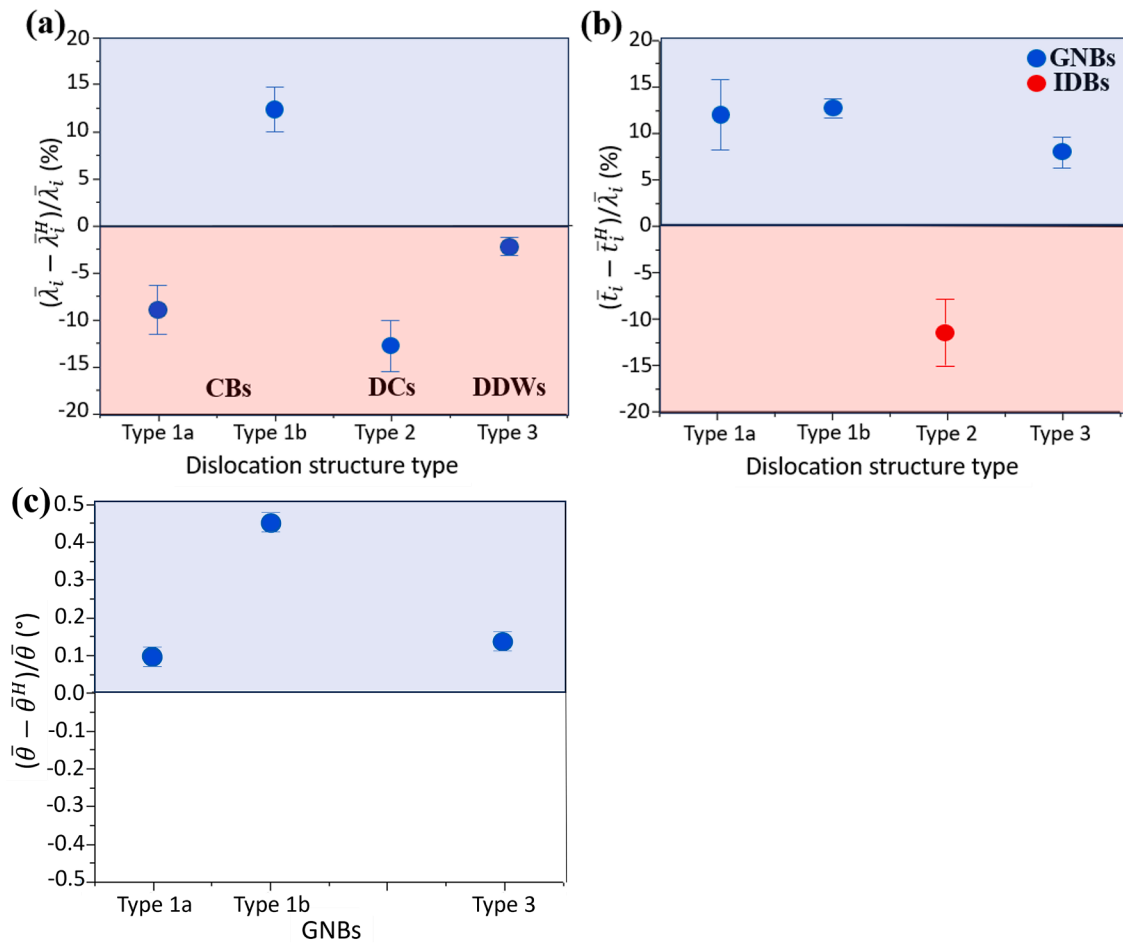


Fig. 15. Hydrogen-induced variations on the average scale of dislocation structure types (a), average boundary thickness (b), and average boundary misorientation (c) of a Fe-19Ni-24Cr steel tensile deformed at $\varepsilon = 0.15$. CBs: Cell blocks; DCs: Dislocation cells; DDWs: Dense dislocation walls; GNBs: Geometrically necessary boundaries; IDBs: Incident dislocation boundaries.

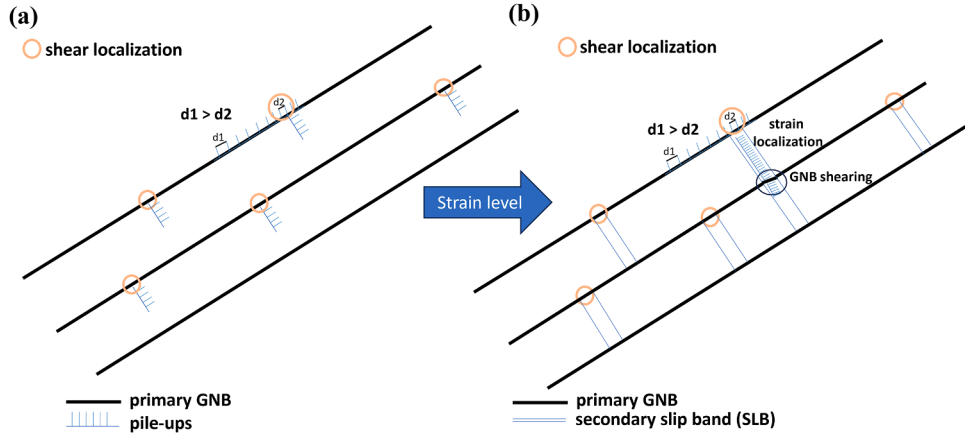


Fig. 16. Schematics of the proposed mechanism for hydrogen-induced secondary slip. (a): Dislocation emission (pile-ups) due to hydrogen-induced shear localization. (b): Propagation of secondary slip bands (SLB) across the GNB structure. d_1 , d_2 : dislocation spacing.

stresses associated with GNBs and DCs on mechanical stress is neglected [26,71,72]. In the following, we analyze the contribution of each hardening term. The contribution of DCs to hardening is given by [54, 55]:

$$\sigma_{DC} = GbKM/\bar{\lambda}_{DC} \quad (4)$$

where G is the shear modulus, b is the Burgers vector, K is the cell similitude constant, M is the Taylor factor, and $\bar{\lambda}_{DC}$ is the average cell size. In this model, the average MFP corresponds to $\bar{\lambda}_{DC}$. The contributions of CBs and DDWs to the strain hardening can be written as Hall-Petch-type relations [73–75]:

$$\sigma_{CB} = \frac{K_{GB}}{\sqrt{\bar{\lambda}_{GNB}}} \quad (5)$$

$$\sigma_{DDW} = \frac{K_{GB}}{\sqrt{\bar{\lambda}_{DDW}}} \quad (6)$$

where K_{GB} is the Hall-Petch constant. $\bar{\lambda}_{GNB}$ and $\bar{\lambda}_{DDW}$ correspond to the average MFP in grains forming Type 1 and Type 3 dislocation structures, respectively. In this approach, DDWs and CB walls are considered as GNBs [33,76,77]. The hardening associated with the different

dislocation structures was calculated by relations (4–6). We assume that the influence of hydrogen on G , b , and K_{GB} is negligible [19,43]. The data used in these calculations were the values of $\bar{\lambda}_{DC}$, $\bar{\lambda}_{GNB}$, and $\bar{\lambda}_{DDW}$ estimated in this study (Table 1), the K -values obtained in this study ($K=3.8$ and $K^H=3.6$), $K_{GB}=280 \text{ MPa } \mu\text{m}^{1/2}$ [56], $G=80 \text{ GPa}$ [35], $b=0.25 \text{ nm}$ [35], and $M=2.45$.

Fig. 17(a) shows the intrinsic mechanical strength of the different types of dislocation structures calculated at $\varepsilon = 0.05$ and $\varepsilon = 0.15$ for the uncharged (red bars) and hydrogen-charged (blue bars) conditions (stages II/III hardening). The plots reveal several hydrogen-related effects on the terms σ_{DC} , σ_{CB} , and σ_{DDW} defined by relations (4–6). Specifically, hydrogen increases σ_{DC} and σ_{Cba} by 15–20 MPa, decreases σ_{Cbb} by 15 MPa, while having a negligible effect on σ_{DDW} . These effects can be explained by the observed limited hydrogen-induced variation on the dislocation structure scale. Notably, the present analysis indicates that the impact of hydrogen on strain hardening exhibits a grain-orientation dependence and hence, is texture-dependent. The influence of hydrogen on the overall mechanical stress associated with the dislocation structure formed at $\varepsilon = 0.15$ is analyzed in Fig. 17(b). The values of σ were calculated by eq. (3) with the data shown in Fig. 17(a), using $\sigma_0 = 175 \text{ MPa}$ [56], $\sigma_0^H = 230 \text{ MPa}$ [35], and the grain fractions estimated from IPFs (Figs. 6(e, f)): $f_{DC} = 0.25$, $f_{Cba} = 0.10$, $f_{Cbb} = 0.05$, and $f_{DDW} = 0.60$.

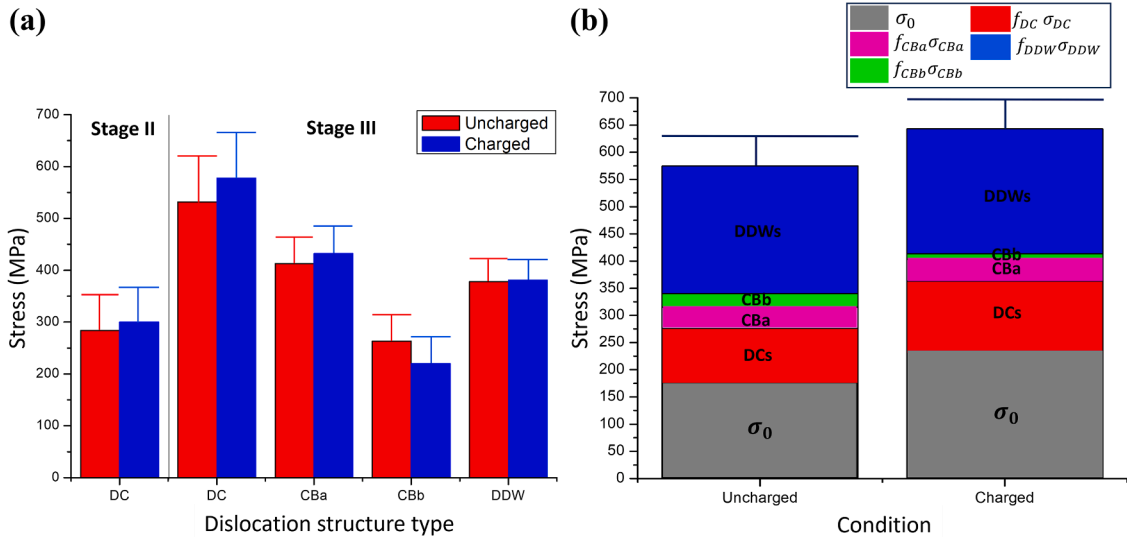


Fig. 17. (a): Intrinsic mechanical strength of the different types of dislocation structures calculated at $\varepsilon = 0.05$ (stage II hardening) and $\varepsilon = 0.15$ (stage III hardening) for the uncharged and hydrogen-charged conditions. DCs: dislocation cells; Cba: Type 1a cell blocks; Cbb: Type 1b CB; DDWs: Dense dislocation walls. (b): Calculated mechanical strength at for the uncharged and hydrogen-charged conditions (stage III hardening).

The calculated mechanical stresses, $\sigma = 575 \text{ MPa} \pm 55 \text{ MPa}$ and $\sigma^H = 645 \pm 55 \text{ MPa}$, are close to the experimental values of $\sigma = 555 \text{ MPa}$ and $\sigma^H = 615 \text{ MPa}$ for $\varepsilon = 0.15$. Several key findings can be drawn from this analysis. First, the contribution of σ_{DC} , σ_{CB} , and σ_{DDW} to the mechanical stress is determined by the grain orientation-dependence of the deformation texture. Accordingly, the strain hardening behavior is mainly determined by the evolution of the Type 3 dislocation structure (DDWs) with strain. Second, σ_0 and σ_{DDW} are the dominant terms of the flow stress. Each term accounts for 32 – 38 % of the total flow stress. The analysis also reveals that the stress term with the strongest dependence on hydrogen addition is the matrix friction stress (σ_0) associated with solid-solution strengthening, increasing by 50 – 55 MPa. Third. Considering that hydrogen has a negligible influence on the deformation texture, and thereby on the grain area fractions f_{DC} , f_{CBa} , f_{CBb} , and f_{DDW} , we estimate that the impact of hydrogen on the individual hardening terms associated with the dislocation structures (relations (4–6)) is less than 5 MPa. This result agrees with the negligible influence of hydrogen on stages II and III hardening (Fig. 5).

The previous analysis has a significant impact on the design of HE-resistant Fe-Ni-Cr austenitic steels. The present study shows that at the current hydrogen content of 133 mass ppm and deformation conditions of room temperature and a strain rate range of $10^{-5} - 10^{-3} \text{ 1/s}$, hydrogen slightly modifies dislocation structure hardening. The hardening term showing the strongest variation with hydrogen corresponds to solute-solution strengthening. This finding indicates that the main impact of hydrogen on the strain hardening of the Fe-19Ni-24Cr steel is associated with solute solution strengthening, increasing the mechanical strength by $\sim 50 \text{ MPa}$. This effect promotes deformation twinning, enhancing the strain hardening capacity by the activation of an additional hardening stage, stage IV hardening (Fig. 5). This effect and the lack of strain localization-induced damage enable superior hydrogen-embrittlement (HE) resistance. This result highlights the interplay between solute hydrogen strengthening and HE resistance, emphasizing the role of hydrogen as a structural parameter for enhancing the strain hardening capacity of Fe-Ni-Cr austenitic steels, due to its positive effect on promoting deformation twinning.

5. Conclusions

We have quantitatively evaluated the influence of a uniform distribution of solute hydrogen (133 mass ppm) on key variables of dislocation structures and strain hardening in a Fe-19Ni-24Cr (wt. %) austenitic steel through quantitative dislocation structure analysis. Statistical analyses of the relevant variables of the dislocation structure were performed with sufficient statistical significance along the main components of the deformation texture by combined electron channeling contrast imaging (ECCI), electron backscatter diffraction (EBSD), and scanning transmission electron microscopy (STEM). The following conclusion can be drawn:

- The influence of hydrogen on dislocation structure variables (scale, boundary thickness, and boundary misorientation) exhibits distinctive grain orientation dependences, associated with the type of dislocation structure (cells, cell blocks, and dense dislocation walls), dislocation boundary nature (geometrically necessary boundary vs. incidental dislocation boundary), and slip class type.
- Hydrogen induces several effects on the deformation behavior associated with the activation of secondary dislocation structures and strain localization. We propose a dislocation-based model that correlates the hydrogen-induced strain accommodation process occurring at cell block boundaries to the activation of secondary slip sources.
- The analysis of strain hardening using a dislocation structure-based statistical model clarifies the effect of hydrogen on the contribution of dislocation cells, cell blocks, and dense dislocation walls to

hardening. We find that the elastic shielding effect has a reduced impact on the long-range elastic interactions between dislocations, limiting the influence of hydrogen on dislocation structure variables and hardening parameter, α , associated with dislocation forest-type hardening. As a consequence, hydrogen slightly modifies dislocation structure hardening. The hardening mechanism most dependent on hydrogen is solid-solution strengthening.

- The limited influence of hydrogen on dislocation plasticity-related phenomena, such as dislocation structure hardening and strain localization-assisted damage, highlights the interplay between solute hydrogen strengthening and hydrogen embrittlement (HE) resistance, due to the positive influence of hydrogen on promoting deformation twinning, enabling a superior strain hardening capacity.

CRedit authorship contribution statement

Ivan Gutiérrez-Urrutia: Writing – review & editing, Writing – original draft, Investigation, Funding acquisition, Conceptualization. **Yuhei Ogawa:** Writing – review & editing. **Akinobu Shibata:** Writing – review & editing.

Declaration of competing interest

The authors declare that they have no known competing financial interests or personal relationships that could have appeared to influence the work reported in this paper.

Acknowledgments

This work was supported by JSPS KAKENHI Grant Nos. 25K08261 and 24K17180. The authors would like to thank Dr. Singh and Mrs. Nakamura for their support with STEM sample preparation and STEM operation. YO would also like to express his sincere gratitude to Mr. Hyuga Hosoi, a former master's course student at Kyushu University, for his dedicated assistance in mechanical testing and sample preparation.

Supplementary materials

Supplementary material associated with this article can be found, in the online version, at [doi:10.1016/j.actamat.2026.122078](https://doi.org/10.1016/j.actamat.2026.122078).

References

- [1] C.S. Marchi, B.P. Somerday, X. Tang, G.H. Schiroky, Effects of alloy composition and strain hardening on tensile fracture of hydrogen precharged type 316 stainless steels, *Int. J. Hydrog. Energy* 33 (2008) 889–894.
- [2] D.G. Ulmer, C.J. Altstetter, Hydrogen-induced strain localization and failure of austenitic stainless steels at high hydrogen concentrations, *Acta Met. Mater.* 39 (1991) 1237–1248.
- [3] D.P. Abraham, C.J. Altstetter, Hydrogen-enhanced localization of plasticity in an austenitic stainless steel, *Met. Mater. Trans. A* 26 (1995) 2859–2871.
- [4] F.D. León-Cázarez, X. Zhou, B. Kagay, J.D. Sugar, C. Alleman, J. Ronevich, C. S. Marchi, Hydrogen effects on the deformation and slip localization in a single crystal austenitic stainless steel, *Int. J. Plast* 180 (2024) 104074.
- [5] I. Aubert, J.-M. Olive, N. Saintier, The effect of internal hydrogen on surface slip localisation on polycrystalline AISI 316L stainless steel, *Mater. Sci. Eng. A* 527 (2010) 5858–5866.
- [6] K.A. Nibur, B.P. Somerday, D.K. Balch, C.S. Marchi, The role of localized deformation in hydrogen-assisted crack propagation in 21Cr-6Ni-9Mn stainless steel, *Acta Mater.* 57 (2009) 3795–3809.
- [7] Y. Yagodzinsky, T. Saukkonen, S. Kilpeläinen, F. Tuomisto, H. Hanninen, Effect of hydrogen on plastic strain localization in single crystals of austenitic stainless steel, *Scr. Mater.* 62 (2010) 155–158.
- [8] H.K. Birnbaum, P. Sofronis, Hydrogen-enhanced localized plasticity—a mechanism for hydrogen-related fracture, *Mater. Sci. Eng. A* 176 (1994) 191–202.
- [9] P. Sofronis, H.K. Birnbaum, Mechanics of the hydrogen-dislocation-impurity interactions—I. Increasing shear modulus, *J. Mech. Phys. Solids* 43 (1995) 49–90.
- [10] T. Matsumoto, J. Eastman, H.K. Birnbaum, Direct observations of enhanced dislocation mobility due to hydrogen, *Scr. Met.* 15 (1981) 1033–1037.
- [11] P. Rozenak, I.M. Robertson, H.K. Birnbaum, HVEM studies of the effects of hydrogen on the deformation and fracture of AISI type 316 austenitic stainless steel, *Acta Met. Mater.* 38 (1990) 2031–2040.

- [12] G.M. Bond, I.M. Robertson, H.K. Birnbaum, Effects of hydrogen on deformation and fracture processes in high-purity aluminium, *Acta Met.* 36 (1988) 2193–2197.
- [13] I.M.A. Ghermaoui, A. Oudriss, A. Metsue, R. Milet, K. Madani, X. Feaugas, Multiscale analysis of hydrogen-induced softening in f.c.c. nickel single crystals oriented for multiple-slips: elastic screening effect, *Sci. Rep.* 9 (2019) 13042.
- [14] I.M. Robertson, H.K. Birnbaum, P. Sofronis, Hydrogen Effects on Plasticity, in: J. P. Hirth, L. Kubin (Eds.), *Dislocations in Solids*, Dislocations in Solids, 15, Elsevier Science, 2009.
- [15] S. Wang, A. Nagao, P. Sofronis, I.M. Robertson, Assessment of the impact of hydrogen on the stress developed ahead of a fatigue crack, *Acta Mater.* 174 (2019) 181–188.
- [16] J.P. Chateau, D. Delafosse, T. Magnin, Numerical simulations of hydrogen–dislocation interactions in fcc stainless steels. Part I: hydrogen–dislocation interactions in bulk crystals, *Acta Mater.* 50 (2002) 1507–1522.
- [17] I.M. Robertson, P. Sofronis, A. Nagao, M.L. Martin, S. Wang, D.W. Gross, K. E. Nygren, Hydrogen embrittlement understood, *Met. Mater. Trans. A* 46 (2015) 2323–2341.
- [18] G. Girardin, C. Huvier, D. Delafosse, X. Feaugas, Correlation between dislocation organization and slip bands: TEM and AFM investigations in hydrogen-containing nickel and nickel-chromium, *Acta Mater.* 91 (2015) 141–151.
- [19] Q. Sun, J. He, A. Nagao, Y. Ni, S. Wang, Hydrogen-prompted heterogeneous development of dislocation structure in Ni, *Acta Mater.* 246 (2023) 118660.
- [20] A.S. Argon, *Strengthening Mechanisms in Crystal Plasticity*, Oxford University Press, 2008.
- [21] R. Madec, B. Devincere, L.P. Kubin, From dislocation junctions to forest hardening, *Phys. Rev. Lett.* 89 (2002) 255508.
- [22] P.M. Anderson, J.P. Hirth, J. Lothe, *Theory of Dislocations*, Cambridge University Press, 2017.
- [23] M. Sauzay, L.P. Kubin, Scaling laws for dislocation microstructures in monotonic and cyclic deformation of fcc metals, *Prog. Mater. Sci.* 56 (2011) 725–784.
- [24] H. Mughrabi, The α -factor in the Taylor flow-stress law in monotonic, cyclic and quasi-stationary deformations: dependence on slip mode, dislocation arrangement and density, *Curr. Opin. Solid State Mater. Sci.* 20 (2016) 411–420.
- [25] I. Gutierrez-Urrutia, D. Raabe, Dislocation and twin substructure evolution during strain hardening of an Fe–22 wt.% Mn–0.6 wt.% C TWIP steel observed by electron channeling contrast imaging, *Acta Mater.* 59 (2011) 6449–6462.
- [26] H. Mughrabi, Dislocation wall and cell structures and long-range internal stresses in deformed metal crystals, *Acta Met.* 31 (1983) 1367–1379.
- [27] Q. Liu, N. Hansen, Geometrically necessary boundaries and incidental dislocation boundaries formed during cold deformation, *Scr. Met. Mater.* 32 (1995) 1289–1295.
- [28] X. Huang, Grain orientation effect on microstructure in tensile-strained copper, *Scr. Mater.* 38 (1998) 1697–1703.
- [29] D.A. Hughes, N. Hansen, D.J. Bammann, Geometrically necessary boundaries, incidental dislocation boundaries and geometrically necessary dislocations, *Scr. Mater.* 48 (2003) 147–153.
- [30] G. Winther, Slip systems extracted from lattice rotations and dislocation structures, *Acta Mater.* 56 (2008) 1919–1932.
- [31] I. Gutierrez-Urrutia, Y. Ogawa, A. Shibata, Hydrogen-enhanced microbanding in an austenitic FeMnAlC low-density steel: effect on hydrogen embrittlement resistance, *Acta Mater.* 280 (2024) 120335.
- [32] I. Gutierrez-Urrutia, Y. Ogawa, A. Shibata, Analysis of the influence of hydrogen on prismatic loops and dislocation dipole structure in an austenitic steel: effect on stacking fault energy, *Inter. J. Hydrog. Energy* 180 (2025) 151741.
- [33] I. Gutierrez-Urrutia, A. Shibata, Effect of deformation temperature on strain localization phenomena in an austenitic Fe–30Mn–6.5Al–0.3C low-density steel, *Acta Mater.* 264 (2024) 119566.
- [34] Y. Ogawa, O. Takakuwa, K. Tsuzaki, Solid-solution hardening by hydrogen in Fe–Cr–Ni-based austenitic steel: temperature and strain rate effects, *Mater. Sci. Eng. A* 879 (2023) 145281.
- [35] Y. Ogawa, H. Hosoi, K. Tsuzaki, T. Redarce, O. Takakuwa, H. Matsunaga, Hydrogen, as an alloying element, enables a greater strength-ductility balance in an Fe–Cr–Ni-based, stable austenitic stainless steel, *Acta Mater.* 199 (2020) 181–192.
- [36] K.H. Lo, C.H. Shek, J.K.L. Lai, Recent developments in stainless steels, *Mater. Sci. Eng. R* 65 (2009) 39–104.
- [37] I. Gutierrez-Urrutia, S. Zaefferer, D. Raabe, Coupling of electron channeling with EBSD: toward the quantitative characterization of deformation structures in the SEM, *JOM* 65 (2013) 1229–1236.
- [38] I. Gutierrez-Urrutia, Analysis of FIB-induced damage by electron channeling contrast imaging in the SEM, *J. Microsc.* 265 (2017) 51–59.
- [39] N. Hansen, New discoveries in deformed metals, *Met. Mater. Trans. A* 32A (2001) 2917–2935.
- [40] A.J. Schwartz, M. Kumar, B.L. Adams, D.P. Field, *Electron Backscatter Diffraction in Materials Science*, Springer, 2009.
- [41] I. Gutierrez-Urrutia, Quantitative analysis of electron channeling contrast of dislocations, *Ultramicroscopy* 206 (2019) 112826.
- [42] I. Gutierrez-Urrutia, Analysis of dislocation configurations in a [0 0 1] fcc single crystal by electron channeling contrast imaging in the SEM, *Microscopy* 66 (2017) 63–67.
- [43] T. Ito, Y. Ogawa, W. Gon, W. Mao, T. Kawasaki, K. Okada, A. Shibata, S. Harjo, Role of solute hydrogen on mechanical property enhancement in Fe–24Cr–19Ni austenitic steel: an in situ neutron diffraction study, *Acta Mater.* 287 (2025) 120767.
- [44] Y. Ogawa, M. Tanaka, T. Fujita, A. Shibata, Thermally activated dislocation motion in hydrogen-alloyed Fe–Cr–Ni austenitic steel revisited via Haasen plot, *Inter. J. Hydrog. Energy* 74 (2024) 170–182.
- [45] I. Gutierrez-Urrutia, S. Zaefferer, D. Raabe, The effect of grain size and grain orientation on deformation twinning in a Fe–22 wt.% Mn–0.6 wt.% C TWIP steel, *Mater. Sci. Eng. A* 527 (2010) 3552–3560.
- [46] S. Wang, A. Nagao, K. Edalati, Z. Horita, I.M. Robertson, Influence of hydrogen on dislocation self-organization in Ni, *Acta Mater.* 135 (2017) 96–102.
- [47] A. Oudriss, X. Feaugas, Length scales and scaling laws for dislocation cells developed during monotonic deformation of (001) nickel single crystal, *Int. J. Plast.* 78 (2016) 187–202.
- [48] E.I. Galindo-Nava, P.E.J. Rivera-Diaz-del-Castillo, A thermodynamic theory for dislocation cell formation and misorientation in metals, *Acta Mater.* 60 (2012) 4370–4378.
- [49] P. Hähner, Statistical mechanics approach to dislocation cell patterning, *Scr. Mater.* 47 (2002) 415–421.
- [50] L. Zisis, K.S. Stopka, M.I. Alam, Z.D. Harris, M.D. Sangid, Modeling the influence of hydrogen on Ni201 plastic behavior through integration of experimental observations and multiobjective optimization, *J. Mech. Phys. Solids* 206 (2026) 106345.
- [51] G. Girardin, C. Huvier, D. Delafosse, X. Feaugas, Correlation between dislocation organization and slip bands: TEM and AFM investigations in hydrogen-containing nickel and nickel-chromium, *Acta Mater.* 91 (2015) 141–151.
- [52] S. Wang, A. Nagao, P. Sofronis, I.M. Robertson, Hydrogen-modified dislocation structures in a cyclically deformed ferritic-pearlitic low carbon steel, *Acta Mater.* 144 (2018) 164–176.
- [53] D. Kuhlmann-Wilsdorf, The LES theory of solid plasticity, in: F.R.N. Nabarro, M. S. Duesbery (Eds.), *Dislocations in Solids*, Dislocations in Solids, 11, 2002.
- [54] D. Kuhlmann-Wilsdorf, J.H.V.D. Merwe, Theory of dislocation cell sizes in deformed metals, *Mater. Sci. Eng.* 55 (1982) 79–83.
- [55] D.L. Holt, Dislocation cell formation in metals, *J. Appl. Phys.* 41 (1970) 3197–3201.
- [56] Y. Wang, Z. Ding, Z. Gao, X. Wang, Fabrication and mechanical properties of fully austenitic gradient nanostructured 310S stainless steel, *J. Mater. Sci.* 57 (2022) 15530–15548.
- [57] X. Feaugas, On the origin of the tensile flow stress in the stainless steel AISI 316L at 300K: back stress and effective stress, *Acta Mater.* 47 (1999) 3617–3632.
- [58] F. Roters, D. Raabe, G. Gottstein, Work hardening in heterogeneous alloys-A microstructural approach based on three internal state variables, *Acta Mater.* 48 (2000) 4181–4189.
- [59] B. Wang, Y. Zhang, D.L. McDowell, T. Zhu, Modeling of crack tip fields and fatigue crack growth in FCC crystals, *J. Mech. Phys. Solids* 188 (2024) 105691.
- [60] C. Nowak, C.D. Spataru, K. Chu, X.W. Zhou, R.B. Sills, Molecular dynamics study of hydrogen Cottrell atmosphere in aluminum: influence of solute-solute interactions in the dislocation core, *Phys. Rev. Mater.* 8 (2024) 055404.
- [61] Z.W. Zhou, F.D. Leon-Cazares, C.S. Marchi, New molecular dynamics studies of hydrogen effects on cross-slip energy barriers in austenitic stainless steels, *Comput. Mater. Sci.* 257 (2025) 113990.
- [62] D. Xie, S. Li, M. Li, Z. Wang, P. Gumbsch, J. Sun, E. M, J. Li, Z. Shan, Hydrogenated vacancies lock dislocations in aluminium, *Nat. Comm.* 7 (2016) 13341.
- [63] M. Koyama, S.M. Taheri-Mousavi, H. Yan, J. Kim, B.C. Cameron, S.S. Moieni-Ardakani, J. Li, C.C. Tasan, Origin of micrometer-scale dislocation motion during hydrogen desorption, *Sci. Adv.* 6 (2020) 1187.
- [64] Z.S. Basinski, T.E. Mitchell, Stresses on secondary systems due to piled-up groups of dislocations of arbitrary orientation, *Phil. Mag.* 13 (121) (1966) 103–114.
- [65] O.L.D. Lange, P.J. Jackson, P.D.K. Nathanson, Stresses and secondary slip between overlapping groups of dislocations, *Acta Met.* 28 (1980) 833–839.
- [66] H.S. Yun, S.K. Jeon, V.H. Dao, Y.-K. Lee, S.H. Nahm, Hydrogen-induced activation of cross slip in Ni-based single crystal superalloy, *Mater. Sci. Eng. A* 913 (2024) 147082.
- [67] U.F. Kocks, H. Mecking, Physics and phenomenology of strain hardening: the FCC case, *Prog. Mater. Sci.* 48 (2003) 171–273.
- [68] U.F. Kocks, A statistical theory of flow stress and work-hardening, *Phil. Mag.* 13 (1966) 541–566.
- [69] E. Nes, Modelling of work hardening and stress saturation in FCC metals, *Prog. Mater. Sci.* 41 (1998) 129–193.
- [70] L. Kubin, B. Devincere, T. Hoc, Modeling dislocation storage rates and mean free paths in face-centered cubic crystals, *Acta Mater.* 56 (2008) 6040–6049.
- [71] H. Mughrabi, On the role of strain gradients and long-range internal stresses in the composite model of crystal plasticity, *Mater. Sci. Eng. A* 317 (2001) 171–180.
- [72] H. Mughrabi, Deformation-induced long-range internal stresses and lattice plane misorientations and the role of geometrically necessary dislocations, *Phil. Mag.* 86 (2006) 4037–4054.
- [73] N. Hansen, D.J. Jensen, Flow stress anisotropy caused by geometrically necessary dislocations, *Acta Met. Mater.* 40 (1992) 3265–3275.
- [74] N. Hansen, Boundary strengthening in undeformed and deformed polycrystals, *Mater. Sci. Eng. A* 409 (2005) 39–45.
- [75] N. Hansen, Boundary strengthening over five length scales, *Adv. Eng. Mater.* 7 (2005) 815–821.
- [76] D. Kuhlmann-Wilsdorf, N. Hansen, Geometrically necessary, incidental and subgrain boundaries, *Scr. Met. Mater.* 25 (1991) 1557–1562.
- [77] N. Hansen, X. Huang, W. Pantleon, G. Winther, Grain orientation and dislocation patterns, *Phil. Mag.* 86 (2006) 3981–3994.